

FORMATION OF AN O-STAR CLUSTER BY HIERARCHICAL ACCRETION IN G20.08-0.14 N

ROBERTO GALVÁN-MADRID^{1,2,3}, ERIC KETO¹, QIZHOU ZHANG¹,
STAN KURTZ², LUIS F. RODRÍGUEZ², AND PAUL T. P. HO^{1,3}

The Astrophysical Journal, 706, 1036, 2009 December 1

ABSTRACT

Spectral line and continuum observations of the ionized and molecular gas in G20.08-0.14 N explore the dynamics of accretion over a range of spatial scales in this massive star-forming region. Very Large Array observations of NH₃ at 4'' angular resolution show a large-scale (0.5 pc) molecular accretion flow around and into a star cluster with three small, bright H II regions. Higher resolution (0.4'') observations with the Submillimeter Array in hot core molecules (CH₃CN, OCS, and SO₂) and the VLA in NH₃, show that the two brightest and smallest H II regions are themselves surrounded by smaller scale (0.05 pc) accretion flows. The axes of rotation of the large and small scale flows are aligned, and the timescale for the contraction of the cloud is short enough, 0.1 Myr, for the large-scale accretion flow to deliver significant mass to the smaller scales within the star formation timescale. The flow structure appears to be continuous and hierarchical from larger to smaller scales.

Millimeter radio recombination line (RRL) observations at 0.4'' angular resolution indicate rotation and outflow of the ionized gas within the brightest H II region (A). The broad recombination lines and a continuum spectral energy distribution (SED) that rises continuously from cm to mm wavelengths, are both characteristic of the class of H II regions known as “broad recombination line objects”. The SED indicates a density gradient inside this H II region, and the RRLs suggest supersonic flows. These observations are consistent with photoevaporation of the inner part of the rotationally flattened molecular accretion flow.

We also report the serendipitous detection of a new NH₃ (3,3) maser.

Subject headings: H II regions — ISM: individual (G20.08-0.14) — masers — stars: formation

1. INTRODUCTION

Massive star-forming regions (MSFRs) with O stars are usually identified by a group of hypercompact (HC) H II or ultracompact (UC) H II regions found together, deeply embedded in a dense molecular cloud (Garay & Lizano 1999; Churchwell 2002; Hoare et al. 2007). That several H II regions are typically found within each star-forming region indicates that massive stars form together in small clusters. Furthermore, the infrared luminosity and radio continuum brightness of the individual H II regions suggest that some of them may themselves contain more than one massive star. Thus, the spatial structure of massive star-forming regions is clustered and hierarchical: the star-forming regions contain a number of separate HC and UC H II regions, each of which may in turn contain a few massive stars.

Low angular resolution, single-dish, molecular line surveys of MSFRs show evidence for large scale contraction of the embedding molecular clouds (Wu & Evans 2003; Klaassen & Wilson 2008). Higher angular resolution observations of some of these regions identify velocity gradients consistent with rotation and inflow. In addition to the accretion flows seen on the large-scale ($\sim 0.3 - 1$ pc) of the embedding molecular cloud (G10.6-0.4: Ho & Haschick 1986, Keto et al. 1987a, Keto 1990; G29.96-0.02: Olmi et al. 2003), accretion flows are also seen on

smaller (≤ 0.1 pc) scales around individual HC and UC H II regions (G10.6-0.4: Keto et al. 1988, Sollins et al. 2005a; W3(OH): Keto et al. 1987b, Keto et al. 1995; W51e2: Zhang & Ho 1997, Young et al. 1998; G28.20-0.05: Sollins et al. 2005b; G24.78+0.08: Beltrán et al. 2004, 2005, 2006, Galván-Madrid et al. 2008; G29.96-0.02: Beuther et al. 2007).

It is unclear how the flows on different length scales are related. In the case of G10.6-0.4, the cluster-scale accretion flow can be traced down from the largest cloud scale to the small scale of the brightest H II region, but it is not known whether this holds for other objects. For example, in a survey of MSFRs, selected on the basis of IRAS colors and specifically excluding those with H II regions, multiple bipolar molecular outflows (implying the presence of accretion flows) are seen in random orientations (Beuther et al. 2002a,b, 2003). The different orientations of these smaller-scale flows suggest separate, individual centers of collapse. This comparison raises the question whether a large-scale coherent flow is required for the formation of the most massive stars, O stars ($M_{\star} > 20 M_{\odot}$) capable of producing bright H II regions, whereas B stars require only smaller scale flows.

It is also unclear what happens in an accretion flow when the inflowing molecular gas reaches the boundary of an embedded H II region. Previous observations suggest that the H II regions in an MSFR that are surrounded by accretion flows, may be best understood as deriving from the continuous ionization of the accretion flow (Keto 2002, 2003, 2007), rather than as a dynamically separate expanding bubble of ionized gas within the flow. Part of the ionized gas may continue to the central star

Electronic address: rgalvan@cfa.harvard.edu

¹ Harvard-Smithsonian Center for Astrophysics, 60 Garden Street, Cambridge MA 02138, USA

² Centro de Radioastronomía y Astrofísica, Universidad Nacional Autónoma de México, Morelia 58090, Mexico

³ Academia Sinica Institute of Astronomy and Astrophysics, P.O. Box 23-141, Taipei 106, Taiwan

or stars and part escapes off the rotationally flattened accretion flow as a photoevaporative outflow perpendicular to the plane of rotation (Hollenbach et al. 1994; Yorke & Welz 1996; Lizano et al. 1996; Johnstone et al. 1998; Lugo et al. 2004). The outflow is accelerated to supersonic speeds by the density gradient maintained by the stellar gravity (Keto 2007). Because the extent of an ionized outflow is generally larger than the region of ionized inflow, in most cases the outflow should be detected more easily than the inflow. H II regions classified as “broad recombination line objects” (BRLO) (Jaffe & Martín-Pintado 1999; Sewilo et al. 2004) show steep density gradients and supersonic flows (Keto et al. 2008), consistent with photoevaporation and acceleration. It is not known whether all BRLO are associated with accretion. If the accretion surrounding an O star cluster is continuous from the largest to the smallest scales, this must be the case.

There are only a handful of radio recombination line (RRL) observations that spatially resolve the ionized flow within an HC H II region. Velocity gradients consistent with outflow and rotation in the ionized gas have been previously reported for W3(OH) (Keto et al. 1995), W51e2 (Keto & Klaassen 2008), and G28.20-0.05 (Sewilo et al. 2008). Observations of the very massive and spatially large G10.6-0.4 H II region made at the VLA in the highest possible angular resolution are able to map the inflowing ionized gas (Keto & Wood 2006).

In order to study the accretion dynamics over a range of scales in a MSFR, from the cluster scale down to the scale of individual HC H II regions and within the ionized gas, we set up a program of radio frequency molecular line, recombination line, and continuum observations at two telescopes and with several different angular resolutions. For this study we chose the massive star formation region G20.08-0.14 North (hereafter G20.08N), identified by three UC and HC H II regions detected in the cm continuum by Wood & Churchwell (1989). The total luminosity of the region is $L \sim 6.6 \times 10^5 L_{\odot}$ for a distance of 12.3 kpc.⁴

Previous observations suggest accretion in the G20.08N cluster. Molecular-line observations show dense gas embedding the H II regions (Turner 1979; Plume et al. 1992). Molecular masers, generally associated with ongoing massive-star formation, have been detected in a number of studies (OH: Ho et al. 1983; H₂O: Hofner & Churchwell 1996; and CH₃OH: Walsh et al. 1998). Klaassen & Wilson (2007, 2008) observed large-scale inward motions consistent with an overall contraction of the embedding molecular cloud. Those authors also observed SiO line profiles suggestive of massive molecular outflows, further evidence for accretion and star formation. The recombination line spectra show broad lines (Garay et al. 1985; Sewilo et al. 2004), pre-

sumably due to large, organized motions in the ionized gas. However, the previous observations do not have the angular resolution and the range of spatial scales needed to confirm the presence of accretion flows and study them in detail.

In this paper we report on several observations of G20.08N and discuss our findings. We confirm active accretion within the cluster. Furthermore, we find that the parsec-scale accretion flow fragments into smaller flows around the individual HC H II regions, and that the gas probably flows from the largest scale down to the smallest scale. This continuous and hierarchical accretion may be necessary to supply enough mass to the small-scale flows to form O-type stars, in contrast to low- and intermediate-mass star-forming regions with stars no more massive than $\sim 20 M_{\odot}$, where isolated accretion flows around individual protostars may be sufficient.

2. OBSERVATIONS

2.1. SMA

We observed G20.08N on 2006 June 25 and July 6 with the Submillimeter Array⁵ (Ho et al. 2004) in its very extended (VEX) configuration. Two sidebands covered the frequency ranges of 220.3 – 222.3 GHz and 230.3 – 232.3 GHz with a spectral resolution of $\approx 0.5 \text{ km s}^{-1}$. The H30 α recombination line ($\nu_0 = 231.9009 \text{ GHz}$) was positioned in the upper sideband⁶. The observations sampled baseline lengths from ≈ 50 to $\lesssim 400 \text{ k}\lambda$, sensitive to a range of spatial scales from $\approx 0.5''$ to $\approx 4.1''$.

The visibilities of each observation were separately calibrated using the SMA’s data calibration program, MIR. Table 1 lists relevant information on the calibrators. We used quasars for the absolute amplitude scale as well as the time-dependent phase corrections and frequency-dependent bandpass corrections. Inspection of the quasar fluxes and comparison with their historical flux densities in the SMA database⁷ suggest that flux calibration is accurate to better than 20%. The calibrated data were exported to MIRIAD for further processing and imaging.

There were enough line-free channels in the 2-GHz passband to subtract the continuum in the (u, v) domain. The line-free continuum was self-calibrated in phase, and the gain solutions were applied to the spectral line data. We list all the identified lines in Table 2. Figure 1 shows the continuum-free spectra across the entire sidebands at the position of the 1.3-mm peak.

To improve the sensitivity, the data were smoothed to a spectral resolution of 2 km s^{-1} . The rms noise in our natural-weighted maps, made from the combined observations of both days, is $\sim 2 \text{ mJy beam}^{-1}$ for the single-sideband continuum and $\sim 30 \text{ mJy beam}^{-1}$ per channel (2 km s^{-1} wide) for the line data.

2.2. VLA

Spectral line observations of NH₃ (J, K) = (2, 2) and (3, 3) at two different angular resolutions were obtained

⁴ Both near and far kinematic distances have been reported for G20.08N. The near value given by Downes et al. (1980) ($d \approx 4.1 \text{ kpc}$) is the most commonly quoted in the previous literature. In contrast, Fish et al. (2003) and Anderson & Bania (2009) report that this region is at the far kinematic distance ($d \approx 12.3 \text{ kpc}$). We will assume the far distance throughout the rest of the paper. For reference, a scale of $0.5''$ corresponds to $\approx 6000 \text{ AU}$ (0.03 pc). The total luminosity of the region was estimated to be $L \sim 7.3 \times 10^4 L_{\odot}$ assuming the near kinematic distance (Wood & Churchwell 1989). Correcting for the location at the far distance, the luminosity is $L \sim 6.6 \times 10^5 L_{\odot}$.

⁵ The Submillimeter Array is a joint project between the Smithsonian Astrophysical Observatory and the Academia Sinica Institute of Astronomy and Astrophysics and is funded by the Smithsonian Institution and the Academia Sinica.

⁶ In “chunk” 20 of the SMA correlator setup

⁷ <http://sma1.sma.hawaii.edu/callist/callist.html>

with the Very Large Array⁸ in the D and BnA configurations (projects AS749, AS771, and AS785). Partial results from these observations were presented in Sollins (2005). All the observations, except the VLA-D (3,3), were done with a bandwidth of 3.125 MHz ($\approx 39 \text{ km s}^{-1}$) divided in 64 spectral channels, each 0.6 km s^{-1} wide. The VLA-D (3,3) observation was done with the same bandwidth divided in 128 spectral channels, each 0.3 km s^{-1} wide. The bandwidth covers the main hyperfine line and one line from the innermost satellite pair⁹. The NH_3 data are presented at a spectral resolution of 0.6 km s^{-1} . The noise per channel in the final images was in the range of $1.0 - 1.5 \text{ mJy beam}^{-1}$.

In addition to the molecular line observations, we observed the ionized gas in the $\text{H}66\alpha$ recombination line in the VLA B configuration. The correlator was set up to cover a bandwidth of 12.5 MHz ($\approx 166 \text{ km s}^{-1}$) divided in 64 channels of 2.6 km s^{-1} each. The rms noise per channel in the final image was $\approx 1 \text{ mJy beam}^{-1}$.

All three VLA data sets were calibrated using standard procedures in the AIPS software. Tables 1 and 2 summarize the relevant observational parameters. The continuum was constructed in the (u, v) domain from line-free channels and was then self-calibrated. The gain solutions from self-calibration were applied to the line data.

3. RESULTS AND DISCUSSION

3.1. The Continuum Emission

3.1.1. Morphology

Figure 2 shows the 1.3-cm continuum (contours) obtained from the VLA-BnA observations overlaid with the 1.3-mm continuum from the SMA-VEX data (color scale). At 1.3 cm we resolve the G20.08N system into the three components reported by Wood & Churchwell (1989). H II region A is the brightest, westernmost peak. H II region B is the slightly broader peak $\approx 0.7''$ to the SE of A. H II region C is the more extended UC H II further to the SE. Its brightest, eastern rim is detected at the $\sim 10 \text{ mJy beam}^{-1}$ level in our 1.3-mm observations.

The continuum of H II region A is unresolved at 1.3 cm; at 1.3 mm it shows a core-halo morphology. The 1.3-mm core is unresolved (Gaussian fits yield a deconvolved size at half power FWHM $\lesssim 0.4''$). The low-intensity halo has a diameter of $\approx 1''$ (see Fig. 2). The $\text{H}30\alpha$ emission is confined to the unresolved core (§ 3.4) and the warm molecular gas (§ 3.3) coincides with the extended continuum halo. This indicates that the unresolved H II region A is surrounded by a dust cocoon. H II region B is barely resolved in the 1.3-cm VLA BnA map (deconvolved FWHM $\approx 0.6''$). The peak position of H II region A is identical at 1.3 cm and 1.3 mm: $\alpha(\text{J2000}) = 18^{\text{h}} 28^{\text{m}} 10^{\text{s}}.30$, $\delta(\text{J2000}) = -11^\circ 28' 47''.8$, within the positional uncertainty of the reference quasars (in the range $0.01'' - 0.1''$).

3.1.2. SED and the Nature of the Millimeter Emission

Previous observations of the recombination lines at 2 and 6 cm (Sewilo et al. 2004) put the H II regions in G20.08N in the class known as “broad recombination line objects” (although those observations did not have sufficient angular resolution to separate H II regions A, B, and C). The large widths in cm-wavelength recombination lines are due to pressure broadening at high gas densities ($> 10^5 \text{ cm}^{-3}$) as well as unresolved supersonic motions (Keto et al. 2008). These H II regions also have continuum spectral energy distributions (SEDs) that increase with frequency through the mm wavelengths, evidence for a steep density gradient in the ionized gas (Franco et al. 2000; Keto 2003; Avalos et al. 2006, 2009; Keto et al. 2008). Our new VLA and SMA observations, at 1.3 cm and 1.3 mm respectively, extend the SED to millimeter wavelengths. We find that the flux density of H II region A continues to rise from cm to mm wavelengths (Fig. 2), and we analyze this characteristic in detail below. The flux densities of H II region B at 1.3 mm ($\approx 93 \text{ mJy}$) and 1.3 cm ($\approx 202 \text{ mJy}$) imply a spectral index (α , where $S_\nu \propto \nu^\alpha$) of $\alpha \sim -0.3$, roughly consistent with the expected index of -0.1 of optically thin gas. H II region C is more extended and most of the 1.3-mm flux is resolved out.

At wavelengths shorter than 1 mm, thermal dust emission contributes significantly to the continuum. We estimate the relative contributions of dust and free-free emission at 1.3 mm from our recombination line observations (described in § 3.4) and the theoretically expected line-to-continuum ratio. In the optically thin limit (a good approximation at 1.3 mm) the free-free line-to-continuum flux ratio S_L/S_C is given by the ratio of the opacities κ_L/κ_C (Gordon & Sorochenko 2002):

$$\left[\frac{\kappa_L}{\text{cm}^{-1}} \right] = \frac{\pi h^3 e^2}{(2\pi m_e k)^{3/2} m_e c} n_1^2 f_{n_1, n_2} \phi_\nu \frac{n_e n_i}{T^{3/2}} \times \exp\left(\frac{E_{n_1}}{kT}\right) \left(1 - e^{-h\nu/kT}\right), \quad (1a)$$

$$\left[\frac{\kappa_C}{\text{cm}^{-1}} \right] = 9.77 \times 10^{-3} \frac{n_e n_i}{\nu^2 T^{3/2}} \left[17.72 + \ln \frac{T^{3/2}}{\nu} \right], \quad (1b)$$

where all the units are in cgs, the physical constants have their usual meanings, $n_1 = 30$ for H 30α , $f_{n_1, n_2} \approx 0.1907 n_1 (1 + 1.5/n_1)$ for α lines, $n_e = n_i$ for hydrogen, $T \approx 8000 - 10\,000 \text{ K}$, and ϕ_ν is the normalized line profile. The main source of uncertainty in equations 1 and 1 is the temperature of the ionized gas. Assuming that the line profile is Gaussian and correcting for 8 % helium in the gas, the expected ratio at the line center is $S_{L,0}/S_C \approx 3.0$ for $T = 8000 \text{ K}$, or $S_{L,0}/S_C \approx 2.3$ for $T = 10\,000 \text{ K}$. The observed ratio is $S_{L,0}/S_C \approx 1.8$. Therefore, assuming that the RRLs are in LTE, the free-free contribution to the 1.3-mm flux of H II region A is $\approx 60\% - 80\%$ for the assumed temperature range.

Figure 3 shows a model SED for H II region A in which 70 % (355 mJy) of the 1.3-mm flux is produced by free-free from an H II region with a density gradient and 30 % (142 mJy) by warm dust. Assuming radiative equilibrium, we set the dust temperature T_d to 230 K, the average temperature of the dense gas at the same scales (§3.3.2). The modeling procedure is described in Keto

⁸ The National Radio Astronomy Observatory is operated by Associated Universities, Inc., under cooperative agreement with the National Science Foundation.

⁹ The NH_3 molecule is symmetric top with inversion, see Ho & Townes (1983) for details.

(2003) and Keto et al. (2008). Table 3 summarizes the model. The total gas mass inferred from the dust emission is too large ($M \sim 35 - 95 M_{\odot}$) for the H II region alone, so most of the dust must be in the cocoon around the H II region. The calculated mass range takes into account uncertainties in the dust emissivity, but not in the temperature.

The density gradient derived for the ionized gas in H II region A is $n_e \propto r^{-\gamma}$, with $\gamma = 1.3$. Equilibrium between recombination and ionization in this model H II region requires an ionizing flux equivalent to an O7.5 star (using the computations of Vacca et al. 1996), although this ionizing flux could be made up of several stars of slightly later spectral type. The model for the SED assumes spherical geometry and a static H II region with no inflow of neutral gas into the H II region. In contrast, H II region A is embedded in a rotationally flattened accretion flow (see § 3.3), so the determination of the stellar spectral type is only approximate.

3.2. The Large-Scale Molecular Cloud

The large-scale molecular cloud is detected by the NH₃ VLA-D observations. From these data we find the presence of a parsec-scale accretion flow surrounding the cluster of H II regions. In § 3.2.1 we first estimate the systemic velocity V_{sys} of the cloud with respect to the local standard of rest (LSR), and then analyze the line velocities to determine rotation and infall following the procedure used in measuring accretion flow velocities in previous papers (e.g., Ho & Haschick 1986; Keto et al. 1987a; Zhang & Ho 1997; Young et al. 1998). In § 3.2.2 we derive the physical properties of the cloud: temperature, mass, ammonia abundance, and density.

3.2.1. Dynamics

Figure 4 shows the channel maps of the $(J, K) = (3, 3)$ main hyperfine line. The most notable feature is a velocity gradient along the major axis of the cloud, consistent with rotation. The redshifted emission is toward the NE, while the blueshifted gas is toward the SW. Also, there is strong absorption against the free-free background of the H II regions at the center of the cloud, which are unresolved at $\sim 4''$ resolution. The separation between the emission peaks on either side of the absorption is $\approx 10''$, or 0.6 pc. The symmetry of the channel maps suggests a systemic velocity of about 42 km s^{-1} . A Gaussian fit to the emission spectrum integrated in a box covering the entire cloud, and clipping out the redshifted absorption, gives a centroid velocity of $42.3 \pm 0.4 \text{ km s}^{-1}$. We adopt a systemic velocity for the parsec-scale cloud of $V_{sys} = 42 \text{ km s}^{-1}$, in agreement with that reported by Plume et al. (1992) (41.9 km s^{-1}) based on observations of CS $J = 7 - 6$.

Figure 5 shows position-velocity (PV) diagrams across cuts at PA = 45° (SW-NE, major axis) and PA = 135° (NW-SE, minor axis). The rotation is seen in the SW-NE cut as a shift in the velocity of the emission contours from one side of the absorption to the other. The velocity offset with respect to V_{sys} seen in the emission contours increases inward, suggesting that the gas rotates faster with decreasing radius.

Under the assumption that the velocity gradient seen in emission along the major axis is dominated by rota-

tion, the redshifted absorption in the PV diagrams (Fig. 5) is also evidence for inward flow toward the central H II regions, as there is an excess of redshifted absorption. This is more clearly seen in Fig. 6, which shows the spectra toward the absorption center. The NH₃ (2,2) main hyperfine absorption peak is redshifted by 2.3 km s^{-1} with respect to the systemic velocity. An infall velocity $V_{inf} \approx 2 \text{ km s}^{-1}$ is also seen in the NH₃ (3,3) line, although the spectrum is contaminated by an NH₃ (3,3) maser (see description in Fig. 6). The maser is confirmed by our high angular resolution NH₃ observations (§ 3.6).

If the rotation were seen edge-on, there would not be a velocity gradient across the H II region along the minor axis (NW-SE). At an oblique viewing angle a velocity gradient along the minor axis is created by the inflow. The velocity gradient along both the minor and major axes (Fig. 5) implies that the rotationally flattened flow is tipped with respect to the line of sight.

3.2.2. Cloud Parameters

The optical depth of the gas can be determined from the brightness ratios of the hyperfine lines. From their optical depth ratio the rotational temperature between the (2,2) and (3,3) transitions can be determined (see Keto et al. 1987a; Mangum et al. 1992, for details of the procedure). This temperature can be considered as a first-order approximation to the kinetic temperature (T_k) of the molecular gas. Danby et al. (1988) suggest that an improved estimate of the kinetic temperature (T_k) is obtained by accounting for the populations in the upper states of the K-ladders rather than assuming that all states above the lowest are negligibly populated. Including this correction, we obtain an average kinetic temperature $T_k \sim 22 \text{ K}$ for the parsec-scale cloud. The high-resolution data discussed in § 3.3 show that higher gas temperatures are found closer to the H II regions.

The mean column density of NH₃ is $N_{NH_3} \sim 2.3 \times 10^{16} \text{ cm}^{-2}$. We can determine the abundance of ammonia $X(NH_3)$ by comparing the NH₃ and H₂ column densities. The mass of the cloud can be estimated from the observed velocity dispersion ($\sigma_V \sim 3.5 \text{ km s}^{-1}$), the radius of the cloud ($R \sim 100\,000 \text{ AU}$), and the virial theorem: $M_{vir} = (5/3G)R\sigma_V^2 \sim 2300 M_{\odot}$. Similarly, from the observed velocity gradient, the rotation velocity is $V_{rot} \sim 4 \text{ km s}^{-1}$ at a radius $R \sim 100\,000 \text{ AU}$. Equating the centripetal and gravitational forces, the gas mass inside R is $M = (RV_{rot}^2)/G \sim 1800 M_{\odot}$. Therefore, we estimate the average column density of H₂ to be $N_{H_2} \sim 5 \times 10^{22} \text{ cm}^{-2}$ and $X(NH_3) \sim 5 \times 10^{-7}$, within a factor of three of the value estimated for G10.6-0.4 (Keto 1990). The mean H₂ density in the large-scale cloud is $n_{H_2} \sim 10^4 \text{ cm}^{-3}$.

3.3. Molecular Gas in The Inner 0.1 pc

Our SMA Very Extended (VEX) and VLA-BnA observations provide a rich view of the molecular environment close to the H II regions. The lines detected with the SMA that have peak intensities $> 300 \text{ mJy beam}^{-1}$ and are not blended with any other line are listed in the top part of Table 2. We follow a similar outline as for the large-scale cloud.

3.3.1. Dynamics

Figure 7 shows the channel maps of OCS $J = 19 - 18$, SO₂ $J(K_a, K_b) = 11(1, 11) - 10(0, 10)$, CH₃CN $J(K) = 12(3) - 11(3)$, and CH₃CN $J(K) = 12(4) - 11(4)$. These maps show that the line emission from these hot-core molecules is considerably brighter around H II region A. All the molecules show a velocity gradient across this source, from the southwest to northeast, in a similar orientation as the larger, cluster-scale flow. We do not detect molecular emission around H II region B. At this high angular resolution we are not sensitive to brightness temperatures of less than ~ 10 K (3σ) for the mm lines.

Figure 8 shows the velocity-integrated intensity (moment 0) and the intensity-weighted mean velocity (moment 1) maps of the four lines previously shown in Fig. 7. The integrated emission of CH₃CN $12(4) - 11(4)$ is brightest in front of the H II region, while for the other molecules the brightness peak is slightly offset from the continuum. These differences reflect the relative brightness of each molecule with respect to the continuum emission of H II region A. The velocity gradient across H II region A is also seen. Figure 9 shows the velocity-integrated (moment 0) and velocity dispersion (moment 2) maps for the same lines as Fig. 8. The line widths increase toward the continuum peak, indicating that unresolved motions increase closer to the H II region.

Figure 10 shows the position-velocity (PV) diagrams for the lines of Figure 7 in cuts at position angles PA = 45° and PA = 135° across the continuum peak of H II region A. The cuts at 45° show the velocity gradient also seen in the channel maps of OCS and both of the CH₃CN lines. The PV diagram of CH₃CN $12(4)-11(4)$ has a feature suggestive of a velocity gradient in the perpendicular direction PA = 135°, with an excess of redshifted emission toward the NW. Consistent with our interpretation of the NH₃ VLA-D data, this suggests inward motion in a rotationally-flattened flow that is seen not quite edge-on. The same redshifted feature is also marginally detected in the lower excitation CH₃CN transition as well as the OCS line. However, the infall signature in emission is only tentative, and a clearer indication of infall at small scales comes from the redshifted NH₃ absorption in the VLA-BnA data (see below).

In general, observational experience suggests that CH₃CN, along with NH₃, is a reliable tracer of high-density molecular mass and accretion flows (Cesaroni et al. 1997; Zhang et al. 1998, 2002; Patel et al. 2005). CH₃CN has recently been detected in the outflow of the nearby low-mass star L1157 (Arce et al. 2008), but at a very low brightness (< 0.03 K). The distribution of the OCS molecule in our observations is very similar to the CH₃CN, but the SO₂ velocities do not show the same pattern, and are more difficult to interpret. The SO₂ may be more easily affected by the excitation conditions, and part of the observed emission could arise from the shocked boundaries of outflows. From Gaussian fits to the CH₃CN $K = 2, 3$, and 4 emission lines at the position of the continuum peak, the systemic velocity at small scales is estimated to be $V_{sys} = 41.8 \pm 0.3$ km s⁻¹. Figure 11 shows the CH₃CN spectra and their Gaussian fits.

At subarcsecond angular resolution, our NH₃ obser-

vations are sensitive to emission of brightness temperature above ~ 200 K. Therefore the thermal NH₃ is detected only in absorption against the bright continuum. As in § 3.2.2, a comparison between the NH₃ absorption line velocity and V_{sys} shows an inward velocity of ≈ 2 km s⁻¹ in front of H II region A (Figure 12). The NH₃ (2,2) absorption line in front of H II region B is redshifted by ~ 2.0 km s⁻¹ with respect to V_{sys} , implying inward motion and accretion toward H II region B as well (Figure 12). The (3,3) absorption in front of H II region B is mixed with NH₃ maser emission (§ 3.6), and the determination of the inward velocity is uncertain. More sensitive observations are needed to constrain the properties of the molecular gas around H II region B.

3.3.2. Core Parameters

We estimate the dynamical mass M (gas plus stars) within the smaller accretion flow in the same way as with the large-scale flow (see § 3.2.2). At a radius $R \sim 5000$ AU the rotation velocity is $V_{rot} \sim 3 - 4$ km s⁻¹. Therefore, $M \sim 50 - 90 M_{\odot}$. This is consistent with the lower limit to the stellar mass, $M_{\star} \approx 35 M_{\odot}$, required for ionization equilibrium (§ 3.1.2). The estimate is also consistent with the gas mass derived from the mm continuum once the free-free contribution has been properly subtracted, $M_{gas} \sim 35 - 95 M_{\odot}$ (§3.1.2). The mean H₂ density is $n_{H_2} \sim 10^6$ cm⁻³.

We derive the temperature in the dense gas surrounding H II region A from the rotational energy diagram of the lines of the CH₃CN $J = 12 - 11$ K-ladders (see e.g., Loren & Mundy 1984; Zhang et al. 1998). Figure 13 shows this diagram for two cases: one considering all the $K = 0, \dots, 7$ lines, and the other including only the $K = 4, \dots, 7$ lines, which have lower optical depths than the low-number K lines (also, the $K = 0, 1$ lines are blended, separated by only 5.8 km s⁻¹). The rotational temperature obtained for the former case is $T_{rot} \sim 403$ K, while for the latter it is $T_{rot} \sim 230$ K. The difference between the two values given above appears to be caused by optical depth effects (the rotational diagram analysis assumes that the emission is optically thin). Although our sensitivity level does not permit us to detect the lines of the isotopologue CH¹³CN and measure the optical depth of the CH₃CN emission, the upper limits are not restrictive ($\tau_{CH_3CN} < 20$). High optical depths are also suggested by the flat slope of the K ladders (Fig. 1). Fitting the K ladders taking into account the opacities (Qiu & Zhang 2009) yields a kinetic temperature close to the lower estimation, $T_k \sim 225$ K, and optical depths are $\gg 1$ (Keping Qiu 2009, personal communication). The rotational temperatures are higher if we use only the brightest pixels instead of averaging over all the emission. This suggests a temperature gradient toward the center of the H II region.

We derive a CH₃CN column density of $N_{CH_3CN} \sim 7.5 \times 10^{15}$ cm⁻² assuming $T_k \sim 230$ K. Comparison of the CH₃CN column density with the dynamical mass implies an abundance $X(\text{CH}_3\text{CN}) \sim 5 \times 10^{-9} - 2 \times 10^{-8}$ for the range of masses quoted above. Abundance estimates in other MSFRs cover a range of values: $\sim 10^{-10}$ inside the Orion hot core and $\sim 10^{-11}$ outside (Loren & Mundy 1984); 10^{-8} inside the Orion hot core and $10^{-9} - 10^{-10}$

in the Orion ridge (Wilner et al. 1994); $\sim 3 \times 10^{-8}$ in Sgr B2(N) (Nummelin et al. 2000); $\sim 1 - 5 \times 10^{-7}$ in W51e1/e2 (Remijan et al. 2004).

The optical depth of NH_3 in absorption toward H II region A is $\tau_{2,2} \sim 4.2$, $\tau_{3,3} \sim 0.9$. The mean column density is $N_{\text{NH}_3} \sim 3.6 \times 10^{16} \text{ cm}^{-2}$. If the ammonia abundance at these small scales is in the range $X(\text{NH}_3) = 2 \times 10^{-6} - 1 \times 10^{-7}$, then the molecular hydrogen column density is $N_{\text{H}_2} \sim 2 \times 10^{22} - 4 \times 10^{23} \text{ cm}^{-2}$. This implies a molecular gas mass of $M_{\text{gas}} \sim 2 - 40 M_\odot$. The kinetic temperature obtained from the NH_3 is $T_k \sim 50 \text{ K}$, considerably cooler than that obtained for CH_3CN and implying that most of the NH_3 column density is further away from the H II region than the CH_3CN .

The distribution of the warm molecular gas around H II region A appears to be rotationally flattened (Figs. 7, 8, 9), but the observed size is slightly larger than the radius at which the accretion flow is expected to become centrifugally supported (i.e., a “disk”), $R_d = GM/V_{\text{rot}}^2 \sim 2000 - 3000 \text{ AU}$ for a star of mass $M_\star = 35 M_\odot$ and $V_{\text{rot}} = 3 - 4 \text{ km s}^{-1}$. Actually, the disk scale matches the size of the H II region (Table 3, §3.4).

The mass-inflow rate toward H II region A can be estimated from the high-resolution NH_3 absorption. From an inflow velocity of $V_{\text{inf}} \approx 2 \text{ km s}^{-1}$ and spherical geometry, the mass-inflow rate is $\dot{M} \sim 1 \times 10^{-3} - 2 \times 10^{-2} M_\odot \text{ yr}^{-1}$ (for the $2 - 40 M_\odot$ of molecular gas detected in ammonia absorption). This estimate may be an upper limit because the hot molecular core is flattened rather than spherical.

3.4. The Ionized Gas: Radio Recombination Lines

In § 3.1.2 we inferred a density gradient inside the HC H II region A. In this section, we derive the internal dynamics of this H II region based on multifrequency RRLs. The mm/sub-mm lines are especially important because they are much less affected by pressure broadening and preferentially trace denser gas. While subarcsecond resolution studies at wavelengths longer than 7 mm have been available for many years (De Pree et al. 1997, 2004; Rodríguez et al. 2009), similar studies at shorter wavelengths have had limited angular resolution (e.g., Jaffe & Martín-Pintado 1999). Keto et al. (2008) presented the first results of high-frequency, high-resolution ($\sim 1''$), multifrequency RRL observations in a sample of 5 MSFRs with similar characteristics to G20.08N A. They were able to separate the contributions of pressure broadening and large-scale motions to the line width, even when the H II regions were unresolved. We follow their procedure to analyze our RRL data.

We observed the $\text{H}30\alpha$ ($\nu_0 = 231.90 \text{ GHz}$) and $\text{H}66\alpha$ ($\nu_0 = 22.36 \text{ GHz}$) lines at subarcsecond angular resolution (see Table 2). Because both the line-to-continuum ratio and the continuum intensity are lower at 22 GHz than at 231 GHz, the $\text{H}66\alpha$ line is much weaker than the $\text{H}30\alpha$ line. This is somewhat alleviated by the better sensitivity of the VLA, but the signal-to-noise ratio (S/N) in the high-frequency line is still better. Figure 14 shows the moment 0 and moment 1 maps of the $\text{H}30\alpha$ line. Although the emission is unresolved at half power, there is a slight indication of a velocity gradient in the ionized gas that agrees (not perfectly) with the rotation

seen in CH_3CN and OCS . Figure 15 shows the $\text{H}30\alpha$ and $\text{H}66\alpha$ spectra toward H II region A and their Gaussian fits. The $\text{H}66\alpha$ line shows evidence of a blueshifted wing, suggesting either inflow or outflow in addition to rotation. Within the uncertainties of the fits, both the $\text{H}66\alpha$ and $\text{H}30\alpha$ lines have the same line width (Table 4).

Assuming that the dynamical broadening Δv_D (caused by turbulence and ordered motions) and the thermal broadening Δv_T are Gaussian, and that the pressure broadening Δv_L is Lorentzian, the RRL has a Voigt profile with line width (Gordon & Sorochenko 2002):

$$\Delta v_V(\nu) \approx 0.534 \Delta v_L(\nu) + (\Delta v_D^2 + \Delta v_T^2 + 0.217 \Delta v_L^2(\nu))^{1/2}, \quad (2)$$

where all the widths are FWHM.

For the $\text{H}30\alpha$ line at 231.9 GHz the pressure broadening is less than the thermal broadening at electron densities below $2 \times 10^8 \text{ cm}^{-3}$ (Keto et al. 2008). Our SED modeling indicates lower densities over most of the HII region. Therefore, the observed line width can be attributed to thermal plus dynamical broadening. The electron temperature T_e in UC H II regions is typically $T_e = 8000 - 10\,000 \text{ K}$, with a small gradient as a function of Galactocentric radius (Afflerbach et al. 1996). We adopt $T_e = 9000 \text{ K}$ ($T_B < 100 \text{ K}$ for $\text{H}30\alpha$ because of the low optical depth and $\lesssim 1$ filling factor), which translates into a thermal FWHM of $\Delta v_T = 20.9 \text{ km s}^{-1}$. Therefore, from Eq. 1, we obtain a dynamical width of $\Delta v_D = 24.8 \text{ km s}^{-1}$. From the velocity gradient (Fig. 14) it is seen that $\sim 6 \text{ km s}^{-1}$ of Δv_D can be in the form of rotation. The rest could be caused by inflowing or outflowing ionized gas, as suggested by the blueshifted ($\sim 2 - 3 \text{ km s}^{-1}$) mean velocities of the RRLs, and by the blue wing in the $\text{H}66\alpha$ spectrum (Fig. 15).

Most of the ionized gas that we see should be outflow. Inflow inside the H II region is expected within the radius where the escape velocity from the star exceeds the sound speed of the ionized gas. This is approximately the Bondi-Parker transonic radius (Keto 2007), $R_b = GM_\star/2c_s^2 = 5.5 \text{ AU } M_\star/M_\odot$, or about 190 AU for H II region A, assuming a sound speed $c_s = 9 \text{ km s}^{-1}$ and stellar mass $M_\star = 35 M_\odot$. H II region A extends out to $\sim 2500 \text{ AU}$, so most of the gas is not gravitationally bound to the star and flows outward. In this model, the outflow is continuously supplied by photoevaporation off the rotationally flattened accretion flow (T. Peters et al. 2009, in preparation). The somewhat misaligned velocity gradient in the ionized gas (Fig. 14) derives from a combination of the rotation and outflow blended together in the observing beam.

3.5. Outflow Tracers

Low angular resolution (HPBW = $14''$), single-dish (JCMT) observations of SiO (8-7) show evidence for large-scale molecular outflows in G20.08N (Klaassen & Wilson 2008). Although the standard outflow tracers $^{12}\text{CO } J = 2 - 1$ and $^{13}\text{CO } J = 2 - 1$ are in our passband, we do not detect any CO in emission. The (u, v) coverage of our SMA-VEX observations is incapable of imaging structures larger than $\sim 4''$; therefore,

the CO emission from the molecular cloud and molecular outflow must be on larger scales. ^{12}CO and ^{13}CO are seen in our data in absorption at the position of H II region A, at several different velocities in the range $V_{LSR} = 42 - 84 \text{ km s}^{-1}$. Some CO absorption features are at the same velocities as the HI absorption features of Fish et al. (2003) and are therefore due to foreground gas that is not related to G20.08N but rather to intervening Galactic spiral arms.

3.6. A New NH_3 (3,3) Maser

A handful of NH_3 masers have been reported in the literature, always associated with massive star formation (e.g., Walsh et al. 2007). Many of the known NH_3 masers are from non-metastable ($J > K$) transitions. The first clear detection of a metastable ($J = K$) NH_3 (3,3) maser was reported by Mangum & Wootten (1994) toward DR 21(OH). Most of the detections point toward a shock excitation origin for the population inversion, inasmuch as the maser spots are invariably associated with outflow indicators such as bipolar CO and/or SiO structures, class I methanol masers, and/or water masers (Mangum & Wootten 1994; Kraemer & Jackson 1995; Zhang & Ho 1995).

We report the serendipitous detection of a new NH_3 (3,3) maser toward G20.08N. The maser spot is relatively weak, and is spatially centered at $\alpha(\text{J2000}) = 18^{\text{h}} 28^{\text{m}} 10^{\text{s}}.346$, $\delta(\text{J2000}) = -11^{\circ} 28' 47''.93$, close in projection to the center of H II region B. The maser spot is spatially unresolved even in uniform weighting maps of the VLA-BnA data (HPBW = $0.48'' \times 0.26''$, PA = -0.8°). If the deconvolved source size is limited to half the beam size, then the peak brightness temperature of the spot is constrained to $T_B > 7 \times 10^3 \text{ K}$. The high intensity, together with the absence of similar emission in our (2,2) maps at high angular resolution, confirm the maser nature of the (3,3) emission. The spectral feature is also very narrow (Fig. 16), typical of maser emission, although it shows evidence of line wings. From a Gaussian fit to the line profile, the velocity of the maser is $V_{\text{maser}} \sim 44.7 \text{ km s}^{-1}$ (accurate only to 20 % – 40 %). The FWHM is $\sim 0.7 \text{ km s}^{-1}$, after deconvolving the channel width of 0.6 km s^{-1} . Owing to its position, it is probable that the maser is excited by H II region B. We do not have sufficient data, however, to assert that it is excited in a shock.

4. HIERARCHICAL ACCRETION IN G20.08N

4.1. The Observations

One of the central questions in star formation is whether star formation is “bimodal”, i.e., whether high-mass and low-mass stars form in a different way (Shu et al. 1987). Analysis of recent observations suggests that accretion flows around protostars of all masses can be explained within the standard model of star formation as a combination of a thin disk inside a rotationally flattened envelope (Kumar & Grave 2007; Molinari et al. 2008; E. Keto & Q. Zhang 2009, in preparation). Of course, once a protostar gains the mass and temperature of an O star, the formation of an H II region within the accretion flow introduces new phenomena (Keto 2002; Keto & Wood 2006; Keto 2007). Yet not all

molecular clouds form massive stars. In a comprehensive survey, Solomon et al. (1987) found that clouds that form low-mass stars are uniformly distributed throughout the Galactic disk, but those that form the clusters of the most massive stars, O stars capable of producing significant H II regions, are associated with the galactic spiral arms. If the formation process is very similar (with the addition of significant ionization for $M_{\star} > 20M_{\odot}$), then the difference may be found in the conditions in the molecular clouds. The observations of G20.08N reported here and of G10.6-0.4 reported previously (Keto 1990; Keto & Wood 2006) suggest that one difference is that the molecular clouds surrounding young clusters of O stars are in a state of overall collapse whereas in star-forming regions without H II regions we see only localized collapse.

In G20.08N the H II regions A, B, and C are surrounded by a common molecular cloud of radius $\sim 0.5 \text{ pc}$ and mass $M \sim 2000 M_{\odot}$, which is rotating with a velocity of $\sim 4 \text{ km s}^{-1}$ and contracting with an inward velocity of $\sim 2 \text{ km s}^{-1}$. This rotation and contraction constitute a large-scale accretion flow. The velocity of the inward flow is about equal to the rotational velocity implying that the gas is approximately in free-fall and not constrained by centrifugal force. Within this larger flow are at least two smaller accretion flows around H II regions A and B. The molecular core around H II region A is bright enough to be detected in hot-core molecules in emission at subarcsecond angular resolution. The radius and mass of this core are 0.05 pc and $\sim 20 M_{\odot}$. Accretion in the core is indicated by rotation at a velocity of 3 or 4 km s^{-1} and contraction of $\sim 2 \text{ km s}^{-1}$. We do not detect molecular emission around H II region B, but the accretion inflow is inferred from NH_3 absorption that is redshifted by $\sim 2 \text{ km s}^{-1}$ with respect to the systemic velocity.

In contrast, star-forming regions that contain only low mass stars or even stars as massive as type B do not appear to have this global collapse of the entire parent cloud. The observations of these regions suggest only localized accretion flows within individual clumps. For example, star-forming regions such as IRAS 19410+2336 (Sridharan et al. 2002; Beuther et al. 2002b, 2003), IRAS 05358+3543 (Beuther et al. 2002a; Leurini et al. 2007), and AFGL 5142 (Zhang et al. 2002, 2007), have bolometric luminosities of at most a few times $10^4 L_{\odot}$, consistent with type B protostars. There are a number of cores of size similar to those in G20.08N, but there is no reported evidence of a larger parsec-scale, accretion flow.

In an analysis of a recent numerical simulation, Vázquez-Semadeni et al. (2009) also find that the formation of massive stars or clusters is associated with large-scale collapse involving thousands of M_{\odot} and accretion rates of $10^{-3} M_{\odot} \text{ yr}^{-1}$. In contrast, low- and intermediate-mass stars or clusters in their simulation are associated with isolated accretion flows that are a factor of 10 smaller in size, mass, and accretion rate.

If global collapse of the host molecular cloud is necessary for the formation of O stars in clusters, then the association of O stars with galactic spiral arms may imply that compression of giant molecular clouds as they pass through galactic spiral arms may be the primary

mechanism for initiating global collapse (Roberts 1969; Shu et al. 1972; Martínez-García et al. 2009). The low-mass star-forming regions found by Solomon et al. (1987) to be spread throughout the Galaxy may not need such large-scale compression.

4.2. Resupply of the Star-Forming Cores

The orientations of the large cloud-scale accretion flow and the core-scale flow around H II region A are similar and the flows could be continuous (we do not know the orientation of the flow around H II region B because we cannot detect the surrounding molecular emission). The molecular core around H II region A contains only a few tens of M_{\odot} , similar to the mass of a single O star. If the core is to form one or more O stars at less than 100 % efficiency, its mass must be resupplied by the larger scale accretion flow. Resupply is also suggested by the short dynamical or crossing timescale, given by the ratio of the size to the infall velocity, $\sim 10^4$ yrs. If the core is to last more than this, it must be resupplied by the larger scale flow, which has a dynamical timescale of $\sim 10^5$ yrs. If the core is not resupplied then the growing protostar may simply run out of gas before reaching the mass of an O star.

A similar process of resupply is suggested in recent theoretical work. Analytic arguments show that as an unstable cloud fragments, there should be a continuous cascade of mass from larger to smaller fragments as well as a cascade of kinetic energy (Field et al. 2008; Newman & Wasserman 1990). In recent numerical simulations of high mass star formation, Wang et al. (2009) find that most of the mass is supplied from outside a 0.1 pc core around the protostar. Vázquez-Semadeni et al. (2009) and T. Peters et al. (2009, in preparation) also find in their simulations that as a massive core is consumed from the inside by an accreting protostar, the core continues to accrete mass from the outside.

4.3. Accretion Rate

The accretion rate within the small-scale flow around H II region A is $\dot{M} \sim 1 \times 10^{-3}$ to $2 \times 10^{-2} M_{\odot}$. Similar accretion rates are reported for flows around other H II regions such as G10.6-0.4, $8 \times 10^{-4} M_{\odot} \text{ yr}^{-1}$ (Keto 1990), and W51e2, 3×10^{-3} to $1 \times 10^{-2} M_{\odot} \text{ yr}^{-1}$ (Young et al. 1998). In contrast, the accretion rates estimated for the cores in these MSFRs without bright H II regions are generally lower by one or two orders of magnitude, $\sim 10^{-4} M_{\odot} \text{ yr}^{-1}$ (Beuther et al. 2002a,b).

A high accretion rate is necessary to form an O star. Because accreting massive protostars begin core hydrogen burning well before reaching the mass of an O star, they evolve essentially as main-sequence stars of equivalent mass. Numerical simulations of stellar evolution that include accretion predict that unless the accretion rate is high enough, a growing massive protostar will evolve off the main-sequence and explode before it reaches the mass of an O star (Keto & Wood 2006). For a protostar to gain the mass of an O star, the rate at which accretion supplies fresh hydrogen to the growing protostar must be greater than the rate at which the star burns the hydrogen. At the upper end of the mass spectrum, $M_{\star} > 40 M_{\odot}$, this rate is $> 10^{-3} M_{\odot} \text{ yr}^{-1}$. The accretion flows in G20.08N are capable of supplying gas at

the rate necessary to form massive O stars. In MSFRs without O stars, the accretion rates may be too low for the stars to achieve the mass of an O star within their hydrogen-burning lifetimes.

4.4. Transfer of Angular Momentum

If the flow in G20.08N is continuous, then the observations show that the flow spins up as it contracts. Ignoring projection effects, the magnitude of the specific angular momentum on the large scale is $L/m \sim 0.6 \text{ km s}^{-1} \text{ pc}$ at $r \approx 0.2 \text{ pc}$, from the VLA-D NH₃ data, while from the VEX SMA data it is $L/m \sim 0.1 \text{ km s}^{-1} \text{ pc}$ at $r \approx 0.02 \text{ pc}$ around H II region A. From these estimates ~ 85 % of the specific angular momentum in the large-scale flow is lost. In previous observations of G10.6-0.4 (Keto 1990), we found that 97% of the angular momentum in that flow is lost between 1.5 and 0.02 pc. Evidently, angular momentum is efficiently transferred outward and does not prevent collapse of the cloud.

Magnetic fields may be important in this process (e.g., Girart et al. 2009). Although there are no observations of the magnetic field in G20.08N, the field direction has been mapped in another MSFR with HC H II regions, W51e1/e2. Here, observations show that the magnetic field is uniform on the larger scale, 0.5 pc (Lai et al. 2001), while on the smaller scale, 0.03 pc, of the accretion flow onto W51e2, the field is pinched into an hourglass shape with the accretion flow at the waist (Tang et al. 2009). Thus ordered field lines extend from the H II region-scale accretion flow to the large-scale molecular cloud, and if the field has enough strength, angular momentum could be transferred outward by the field. However, dust polarization observations do not give a direct estimate of the field strength, and it is also possible that the field is essentially passive and just carried along by the flow. The observation that the clouds in both W51e1/e2 and G20.08N are close to free-fall collapse implies that the magnetic field is not strong enough to support the clouds. In other words, these clouds are magnetically supercritical.

Numerical simulations of star formation that do not include magnetic forces show that angular momentum can be transferred by hydrodynamics alone. Abel et al. (2002) find that at any radius, there is both low and high angular momentum gas, and that pressure forces or shock waves can redistribute the angular momentum between fluid elements. Lower angular momentum gas sinks inward and displaces higher angular momentum gas outward, resulting in a net outward flow of angular momentum.

Whether the specific angular momentum is transferred by hydrodynamics or magnetic forces, observations and simulations show that angular momentum is not conserved as a function of radius, and does not prevent the gas from flowing continuously from large to small scales in a rotating flow.

5. CONCLUSIONS

We report radio and mm observations of the molecular and ionized gas toward the O-star cluster G20.08N, made with an angular resolution from $\sim 0.1 \text{ pc}$ to $\sim 0.01 \text{ pc}$. Our main findings can be summarized as follows:

1. We find a large-scale ($\sim 0.5 \text{ pc}$) accretion flow

- around and into a star cluster with several O-type stars, identified by one UC and two HC H II regions. This flow is rotating and infalling towards its center. The two HC H II regions are surrounded by smaller accretion flows (~ 0.05 pc), each of them with the signature of infall too. The brightest (toward H II region A) is detected in mm emission lines, and rotates in concordance with the large-scale flow.
2. The similar orientations of the flows at small and large scales, as well as their dynamical timescales ($\sim 10^4$ yrs and $\sim 10^5$ yrs respectively), and masses ($\sim 10 M_{\odot}$ and $\sim 10^3 M_{\odot}$ respectively), suggest that, if O stars are forming in G20.08N (as it is observed), then the smaller scales ought to be resupplied from the larger scales. The same result has been found in recent numerical simulations of massive star formation in clusters.

3. The brightest HC H II region (A) has a rising SED from cm to mm wavelengths and broad hydrogen recombination lines. Both characteristics suggest density gradients and supersonic flows inside the H II region. A tentative velocity gradient is detected in the recombination line emission of this source, suggesting rotation and outflow in the ionized gas at the innermost scales. H II region A can be interpreted as the inner part of the surrounding molecular accretion flow, with the observed ionization being produced by photoevaporation.

We thank the anonymous referee for a detailed report. We also thank Keping Qiu for his comments on the temperature determination. R. G.-M. acknowledges support from an SMA predoctoral fellowship.

REFERENCES

- Abel, T., Bryan, G.L., & Norman, M.L., 2002, *Science*, 295, 93
 Afflerbach, A., Churchwell, E., Acord, J. M., Hofner, P., Kurtz, S., & Depree, C. G. 1996, *ApJS*, 106, 423
 Anderson, L. D., & Bania, T. M. 2009, *ApJ*, 690, 706
 Arce, H. G., Santiago-García, J., Jørgensen, J. K., Tafalla, M., & Bachiller, R. 2008, *ApJ*, 681, L21
 Avalos, M., Lizano, S., Franco-Hernández, R., Rodríguez, L. F., & Moran, J. M. 2009, *ApJ*, 690, 1084
 Avalos, M., Lizano, S., Rodríguez, L. F., Franco-Hernández, R., & Moran, J. M. 2006, *ApJ*, 641, 406
 Beltrán, M. T., Cesaroni, R., Neri, R., Codella, C., Furuya, R. S., Testi, L., Olmi, L. 2004 *ApJ*, 601, L187
 Beltrán, M. T., Cesaroni, R., Neri, R., Codella, C., Furuya, R. S., Testi, L., & Olmi, L. 2005, *A&A*, 435, 901
 Beltrán, M. T., Cesaroni, R., Codella, C., Testi, L., Furuya, R. S., & Olmi, L. 2006, *Nature*, 443, 427
 Beuther, H., Schilke, P., Gueth, F., McCaughrean, M., Andersen, M., Sridharan, T. K., & Menten, K. M. 2002a, *A&A*, 387, 931
 Beuther, H., Schilke, P., Sridharan, T. K., Menten, K. M., Walmsley, C. M., Wyrowski, F. 2002b, *A&A*, 383, 892
 Beuther, H., Schilke, P., & Stanke, T. 2003, *A&A*, 408, 601
 Beuther, H., Zhang, Q., Bergin, E. A., Sridharan, T. K., Hunter, T. R., & Leurini, S. 2007, *A&A*, 468, 1045
 Cesaroni, R., Felli, M., Testi, L., Walmsley, C. M., & Olmi, L. 1997, *A&A*, 325, 725
 Churchwell, E. 2002, *ARA&A*, 40, 27
 Danby, G., Flower, D. R., Valiron, P., Schilke, P., & Walmsley, C. M. 1988, *MNRAS*, 235, 229
 De Pree, C. G., Mehringer, D. M., & Goss, W. M. 1997, *ApJ*, 482, 307
 De Pree, C. G., Wilner, D. J., Mercer, A. J., Davis, L. E., Goss, W. M., & Kurtz, S. 2004, *ApJ*, 600, 286
 Downes, D., Wilson, T. L., Bieging, J., & Wink, J. 1980, *A&AS*, 40, 379
 Field, G. B., Blackman, E. G., & Keto, E. R. 2008, *MNRAS*, 385, 181
 Fish, V. L., Reid, M. J., Wilner, D. J., & Churchwell, E. 2003, *ApJ*, 587, 701
 Franco, J., Kurtz, S., Hofner, P., Testi, L., García-Segura, G., & Martos, M. 2000, *ApJ*, 542, L143
 Galván-Madrid, R., Rodríguez, L. F., Ho, P. T. P., & Keto, E. 2008, *ApJ*, 674, L33
 Garay, G., & Lizano S. 1999, *PASP*, 111, 1049
 Garay, G., Reid, M. J., & Moran, J. M. 1985, *ApJ*, 289, 681
 Girart, J. M., Beltrán, M. T., Zhang, Q., Rao, R., & Estalella, R. 2009, *Science*, 324, 1408
 Gordon, M. A., & Sorochenko, P. N. 2002, *Radio Recombination Lines: Their Physics and Astronomical Applications* (Dordrecht: Kluwer)
 Ho, P. T. P., & Haschick, A. D. 1986, *ApJ*, 304, 501
 Ho, P. T. P., Moran, J. M., & Lo, K. Y. 2004, *ApJ*, 616, L1
 Ho, P. T. P., Vogel, S. N., Wright, M. C. H., & Haschick, A. D. 1983, *ApJ*, 265, 295
 Ho, P. T. P., & Townes C. H. 1983, *ARA&A*, 21, 239
 Hoare, M. G., Kurtz, S. E., Lizano, S., Keto, E., & Hofner, P. 2007, in *Protostars and Planets V*, ed. B. Reipurth, D. Jewitt, & K. Keil (Tucson: Univ. Arizona Press), 181
 Hofner, P., & Churchwell, E. 1996, *A&AS*, 120, 283
 Hollenbach, D., Johnstone, D., Lizano, S., & Shu, F. 1994, *ApJ*, 428, 654
 Jaffe, D. T., & Martín-Pintado, J. 1999, *ApJ*, 520, 162
 Johnstone, D., Hollenbach, D., & Bally, J., 1998, *ApJ*, 499, 758
 Keto, E. 1990, *ApJ*, 355, 190
 Keto, E. 2002, *ApJ*, 580, 980
 Keto, E. 2003, *ApJ*, 599, 1196
 Keto, E. 2007, *ApJ*, 666, 976
 Keto, E., Ho, P. T. P., & Haschick, A. D. 1987a, *ApJ*, 318, 712
 Keto, E., Ho, P. T. P., & Haschick, A. D. 1988, *ApJ*, 324, 920
 Keto, E., Ho, P. T. P., & Reid, M. J. 1987b, *ApJ*, 323, L117
 Keto, E., & Klaassen, P. 2008, *ApJ*, 678, L109
 Keto, E., Welch, W., Reid, M., & Ho, P.T.P. 1995, *ApJ*, 444, 765
 Keto, E., & Wood, K. 2006, *ApJ*, 637, 850
 Keto, E., Zhang, Q., & Kurtz, S. 2008, *ApJ*, 672, 423
 Klaassen, P. D., & Wilson, C. D. 2007, *ApJ*, 663, 1092
 Klaassen, P. D., & Wilson, C. D. 2008, *ApJ*, 684, 1273
 Kraemer, K. E., & Jackson, J. M. 1995, *ApJ*, 439, L9
 Kumar M.S.N., & Grave, J.M.C., 2007, *A&A*, 472, 155
 Lai, S.-P., Crutcher, R.M., Girart, J.M., & Rao, R., 2001, *ApJ*, 561, 864
 Leurini, S., Beuther, H., Schilke, P., Wyrowski, F., Zhang, Q., & Menten, K. M. 2007, *A&A*, 475, 925
 Lizano, S., Canto, J., Garay, G., & Hollenbach, D., 1996, *ApJ*, 465, 216
 Loren, R. B., & Mundy L. G. 1984, *ApJ*, 286, 232
 Lugo, J., Lizano, S., & Garay, G. 2004, *ApJ*, 614, 807
 Mangum, J. G., & Wootten, A. 1994, *ApJ*, 428, L33
 Mangum, J. G., Wootten, A., & Mundy, L. G. 1992, *ApJ*, 388, 467
 Martínez-García, E. E., González-Lópezlira, R. A., & Bruzual-A, G., 2009, *ApJ*, 694, 512
 Molinari, S., Pezzuto, S., Cesaroni, R., Brand, J., Faustini, F., & Testi, L. 2008, *A&A*, 481, 345
 Newman, W. I., & Wasserman, I. 1990, *ApJ*, 354, 411
 Nummelin, A., Bergman, P., Hjalmarsen, Å., Friberg, P., Irvine, W. M., Millar, T. J., Ohishi, M., & Saito, S. 2000, *ApJS*, 128, 213
 Olmi, L., Cesaroni, R., Hofner, P., Kurtz, S., Churchwell, E., & Walmsley, C. M. 2003, *A&A*, 407, 225O
 Patel, N. et al. 2005, *Nature*, 437, 109
 Plume, R., Jaffe, D. T., & Evans, N. J. 1992, *ApJS*, 78, 505
 Qiu, K., & Zhang, Q. 2009, *ApJ*, 702, L66
 Remijan, A., Sutton, E. C., Snyder, L. E., Friedel, D. N., Liu, S.-Y., & Pei, C.-C. 2004, *ApJ*, 606, 917
 Rodríguez, L. F., Zapata, L., & Ho, P. T. P. 2009, *ApJ*, 692, 162
 Roberts, W.W., 1969, *ApJ*, 158, 123
 Sewilo, M., Churchwell, E., Kurtz, S., Goss, W. M., & Hofner, P. 2004, *ApJ*, 605, 285
 Sewilo, M., Churchwell, E., Kurtz, S., Goss, W. M., & Hofner, P. 2008, *ApJ*, 681, 350
 Shu, F.H., Milione, V., Gebel, W., Yuan, C., Goldsmith, D.W., & Roberts, W.W., 1972, *ApJ*, 173, 557
 Shu, F. H., Adams, F. C., & Lizano, S. 1987, *ARA&A*, 25, 23
 Sollins, P. K. 2005, PhD thesis, Harvard University, ISBN: 3-936586-35-7
 Sollins, P. K., Zhang, Q., Keto, E., & Ho, P. T. P. 2005a, *ApJ*, 624, L49

- Sollins, P. K., Zhang, Q., Keto, E., & Ho, P. T. P. 2005b, *ApJ*, 631, 399
- Solomon, P. M., Rivolo, A. R., Barrett, J., & Yahil, A. 1987, *ApJ*, 319, 730
- Sridharan, T. K., Beuther, H., Schilke, P., Menten, K. M., & Wyrowski, F. 2002, *ApJ*, 566, 931
- Tang, Y.-W., Ho, P.T.P., Koch, P.M., Girart, J.M., Lai, S.-P., & Rao, R., 2009, *ApJ*, 700, 251
- Turner, B. E. 1979, *A&AS*, 37, 1
- Vacca, W. D., Garmany, C. D., & Shull, J. M. 1996, *ApJ*, 460, 914
- Vázquez-Semadeni, E., Gomez, G.C., Jappsen, A.K., Ballesteros-Paredes, J., & Klessen, R.S., 2009, arXiv:0904.4515
- Walsh, A. J., Burton, M. G., Hyland, A. R., & Robinson, G. 1998, *MNRAS*, 301, 640
- Walsh, A. J., Longmore, S. N., Thorwirth, S., Urquhart, J. S., & Purcell, C. R. 2007, *MNRAS*, 382, L35
- Wang, P., Li, Z.-Y., Abel, T., & Nakamura, F. 2009, arXiv:0908.4129
- Wilner, D. J., Wright, M. C. H., & Plambeck, R. L. 1994, *ApJ*, 422, 642
- Wood, D. O. S., & Churchwell, E. 1989, *ApJS*, 69, 831
- Wu, J., & Evans, N. J., II 2003, *ApJ*, 592, L79
- Young, L. M., Keto, E., & Ho, P. T. P. 1998, *ApJ*, 507, 270
- Yorke, H. & Welz, A., 1996, *A&A*, 315, 555
- Zhang, Q., & Ho, P. T. P. 1995, *ApJ*, 450, L63
- Zhang, Q., & Ho, P. T. P. 1997, *ApJ*, 488, 241
- Zhang, Q., Ho, P. T. P., & Ohashi, N. 1998, *ApJ*, 494, 636
- Zhang, Q., Hunter, T. R., Beuther, H., Sridharan, T. K., Liu, S.-Y., Su, Y.-N., Chen, H.-R., & Chen, Y. 2007, *ApJ*, 658, 1152
- Zhang, Q., Hunter, T. R., Sridharan, T. K., & Ho, P. T. P. 2002, *ApJ*, 566, 982

TABLE 1
 OBSERVATIONAL PARAMETERS

Epoch	Array	Phase Center ^a		Bandpass Calibrator	Phase Calibrator	Flux Calibrator
		α (J2000)	δ (J2000)			
2003 Apr 28	VLA-D	18 28 10.384	-11 28 48.65	3C454.3	1833 - 210	0137 + 331
2003 May 13	VLA-D	18 28 10.384	-11 28 48.65	3C454.3	1851 + 005	1331 + 305
2003 Oct 09	VLA-BnA	18 28 10.384	-11 28 48.65	3C454.3	1851 + 005	1331 + 305
2003 Oct 10	VLA-BnA	18 28 10.384	-11 28 48.65	3C454.3	1851 + 005	1331 + 305
2006 Jun 25	SMA-VEX	18 28 10.38	-11 28 48.60	3C273	1830 + 063	1830 + 063
2006 Jun 25	SMA-VEX	18 28 10.76	-11 29 27.60	3C273	1830 + 063	1830 + 063
2006 Jul 06	SMA-VEX	18 28 10.38	-11 28 48.60	3C454.3	1751 + 096	1751 + 096
2006 Jul 06	SMA-VEX	18 28 10.76	-11 29 27.60	3C454.3	1751 + 096	1751 + 096
2007 Oct 26	VLA-B	18 28 10.400	-11 28 49.00	3C454.3	1743 - 038	1331 + 305
2007 Oct 27	VLA-B	18 28 10.400	-11 28 49.00	3C454.3	1743 - 038	1331 + 305

^a Units of right ascension are hours, minutes, and seconds. Units of declination are degrees, arcminutes, and arcseconds.

 TABLE 2
 LINES^a

Species	Transition	ν_0 (GHz)	Array	HPBW (arcsec \times arcsec; deg)
H	66 α	22.364178	VLA-B	0.47 \times 0.34; 3
NH ₃	(2, 2)	23.722633	VLA-D	4.68 \times 2.93; 236
NH ₃	(3, 3)	23.870129	VLA-D	4.50 \times 3.32; 8
NH ₃	(2, 2)	23.722633	VLA-BnA	0.37 \times 0.28; 343
NH ₃	(3, 3)	23.870129	VLA-BnA	0.71 \times 0.34; 0
¹³ CO	2-1	220.398681	SMA-VEX	0.55 \times 0.41; 32
CH ₃ CN	12(4)-11(4)	220.679297	SMA-VEX	0.55 \times 0.41; 32
CH ₃ CN	12(3)-11(3)	220.709024	SMA-VEX	0.55 \times 0.41; 32
CH ₃ CN	12(2)-11(2)	220.730266	SMA-VEX	0.55 \times 0.41; 32
SO ₂	11(1,11)-10(0,10)	221.965200	SMA-VEX	0.54 \times 0.41; 32
CO	2-1	230.538000	SMA-VEX	0.53 \times 0.39; 37
OCS	19-18	231.060991	SMA-VEX	0.53 \times 0.39; 37
H	30 α	231.9009	SMA-VEX	0.53 \times 0.39; 37
CH ₃ CN	12(7)-11(7)	220.539340	SMA-VEX	0.55 \times 0.41; 32
HNCO	10(1,9)-9(1,8)	220.584762	SMA-VEX	0.54 \times 0.41; 32
CH ₃ CN	12(6)-11(6)	220.594438	SMA-VEX	0.55 \times 0.41; 32
CH ₃ CN	12(5)-11(5)	220.641096	SMA-VEX	0.55 \times 0.41; 32
CH ₃ CN	12(1)-11(1)	220.743015	SMA-VEX	0.55 \times 0.41; 32
CH ₃ CN	12(0)-11(0)	220.747265	SMA-VEX	0.55 \times 0.41; 32
CH ₂ CHCN	24(0,24)-23(0,23)	221.76598	SMA-VEX	0.55 \times 0.41; 32
¹³ CS	5-4	231.220768	SMA-VEX	0.52 \times 0.39; 37

^a Detected lines at $S/N > 6$. The *top* part of the table lists the lines with $S/N > 10$ (except the H66 α line) and clearly isolated in frequency. The *bottom* part of the table lists the lines detected at $S/N < 10$ or blended. Some spectral features (see Fig. 1) that were not properly identified due to low S/N (≈ 5) and blending are not listed.

TABLE 3
MODEL FOR THE H II REGION G20.08N A

Parameter ^a	Value
HII Radius (AU)	2530
Electron density ^b (10^5 cm^{-3})	1.4
Exponent ^c	1.3
Gas Mass ^d (M_{\odot})	35-95
Spectral Type	O7.5
Stellar Mass (M_{\odot})	34
HII Mass (M_{\odot})	0.05

^a The independent parameters are the first four rows.

^b Electron density at the HII radius.

^c Exponent γ of the power-law density gradient in the ionized gas, where $n \propto r^{-\gamma}$.

^d Mass of molecular gas obtained from the dust emission. Assuming dust temperature $T_d = 230 \text{ K}$ and a gas-to-dust ratio of 100. The range is caused by the dust emissivity coefficient β used (see Keto et al. 2008), from $\beta = 1$ to $\beta = 1.5$.

TABLE 4
EMISSION LINE PARAMETERS TOWARD H II REGION A^a

Species	Transition	V_{LSR} (km s^{-1})	FWHM (km s^{-1})	$T_{B,peak}$ (K)
H	66α	39.3 ± 1.1	34.1 ± 2.5	190 ± 13
H	30α	40.3 ± 0.4	32.5 ± 0.9	89 ± 2
CH ₃ CN	12(4)-11(4)	42.7 ± 0.3	5.8 ± 0.7	32 ± 4
CH ₃ CN	12(3)-11(3)	41.4 ± 0.2	5.3 ± 0.5	41 ± 4
CH ₃ CN	12(2)-11(2)	41.4 ± 0.2	4.9 ± 0.5	32 ± 3

^a From Gaussian fits. 1σ statistical errors are quoted.

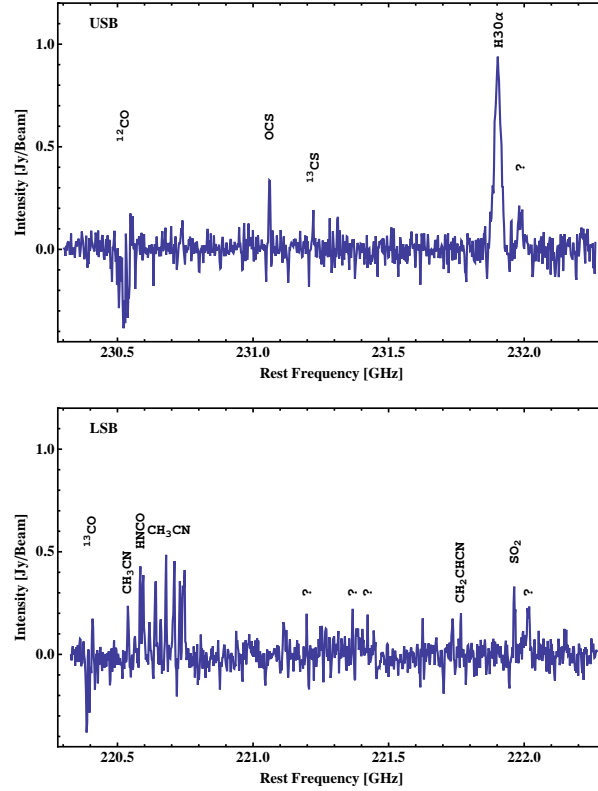


FIG. 1.— Wide-band, continuum-free spectra from the SMA-VEX data at the position of the 1.3-mm continuum peak (see Table 2 for details). The channel spacing in this plot is 3 km s^{-1} . The question mark (?) in the upper sideband (*top* frame) might be a superposition of lines of CH_3OCH_3 and $\text{CH}_3\text{CH}_2\text{CN}$. The ?s at the center of the lower sideband (*bottom* frame) could be from vibrationally excited CH_3CN . The ? in the upper sideband close to the SO_2 might be from CH_3CCH .

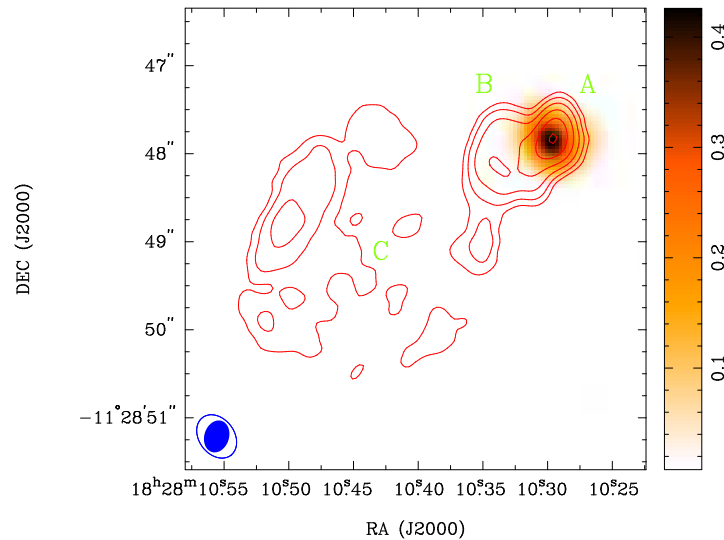


FIG. 2.— VLA-BnA 1.3-cm continuum (*red contours*) overlaid on the SMA-VEX 1.3-mm continuum (*color scale*) toward the G20.08N complex. From west to east: H II region A is the compact, strongest peak at both wavelengths. H II region B is the less bright H II region at $\lesssim 1''$ to the SE of A. H II region C is the more extended emission to the SE of B. The color scale goes linearly from 8 to $430 \text{ mJy beam}^{-1}$ (the rms noise in the mm image is 2 mJy beam^{-1}). Contours are placed at $-5, 5, 10, 20, 40, 80, 150 \times 1 \text{ mJy beam}^{-1}$, the noise of the cm image. The SMA-VEX beam (empty ellipse) encircles the VLA-BnA beam (filled ellipse) at the bottom-left of the image.

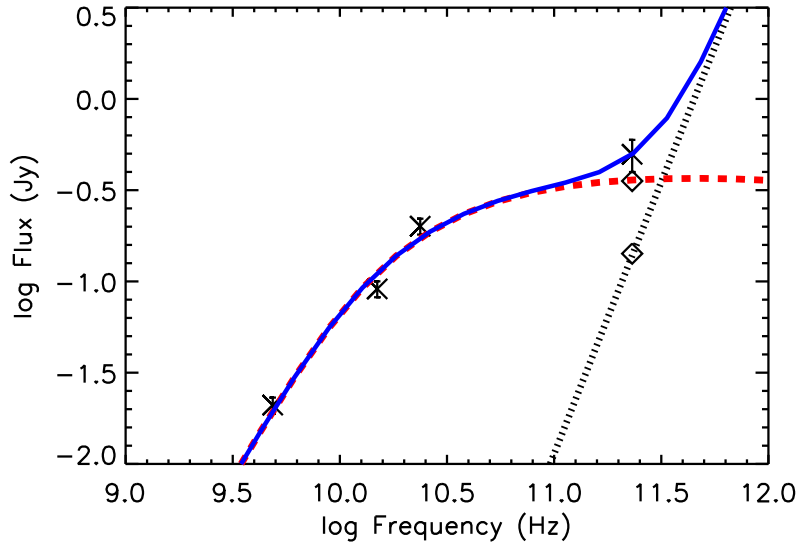


FIG. 3.— Radio-to-millimeter SED of G20.08N A. The 6-cm and 2-cm measurements were obtained from Wood & Churchwell (1989). The 1.3-cm and 1.3-mm points were obtained from Gaussian fits to our VLA-BnA and SMA-VEX data, respectively. *Crosses* are the data points. The error bars correspond to the 10% and 20% uncertainty expected in the VLA and SMA flux measurements, respectively. The *red dashed* line shows the flux of an H II region with a density gradient. The *black dotted* line is the flux from the warm dust component. The *solid blue* line is the sum of the two components. The relative contributions of free-free (70 %) and dust (30 %) to the 1.3-mm flux were estimated from the observed H30 α line-to-continuum ratio, and are marked with *diamonds*.

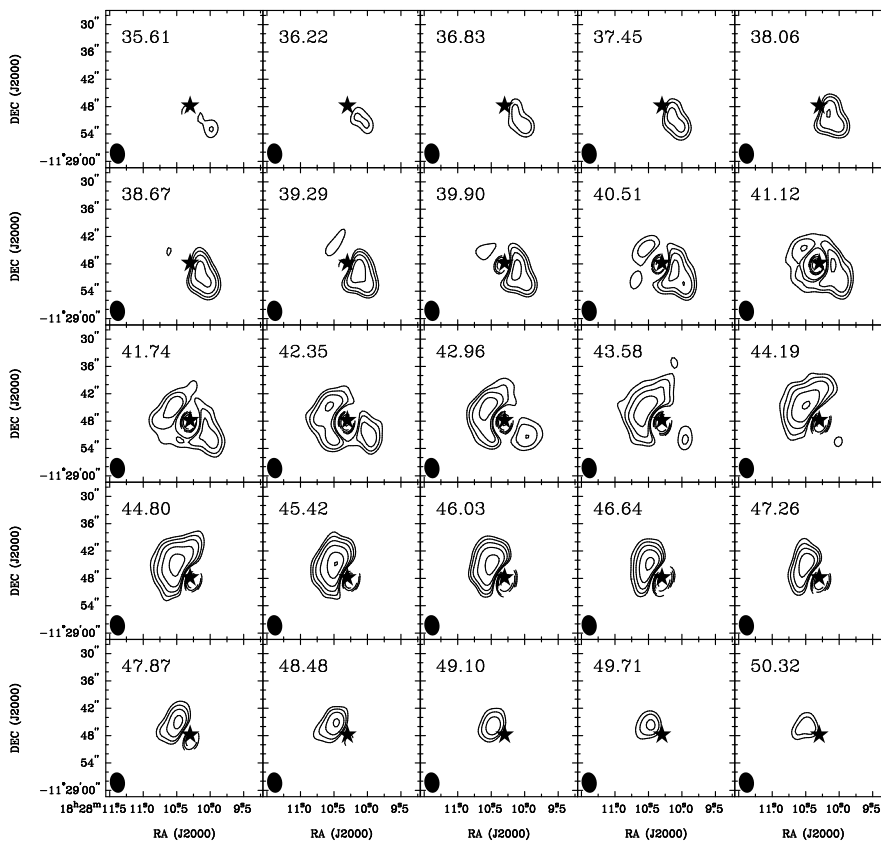


FIG. 4.— Channel maps of the VLA-D NH₃ (3,3) observations. Emission is in *solid* contours and absorption in *dashed* contours. The star covers the H II regions shown in Fig. 1. Contour levels are at $-35, -25, -15, -10, -7, -5, 5, 7, 10, 15, 25, 35 \times 2 \text{ mJy beam}^{-1}$. A clear velocity gradient in emission is seen from one side of the absorption to the other. The LSR systemic velocity of the molecular gas is $V_{sys} = 42.0 \text{ km s}^{-1}$. The original maps at 0.3 km s^{-1} spectral resolution were smoothed to 0.6 km s^{-1} for clarity.

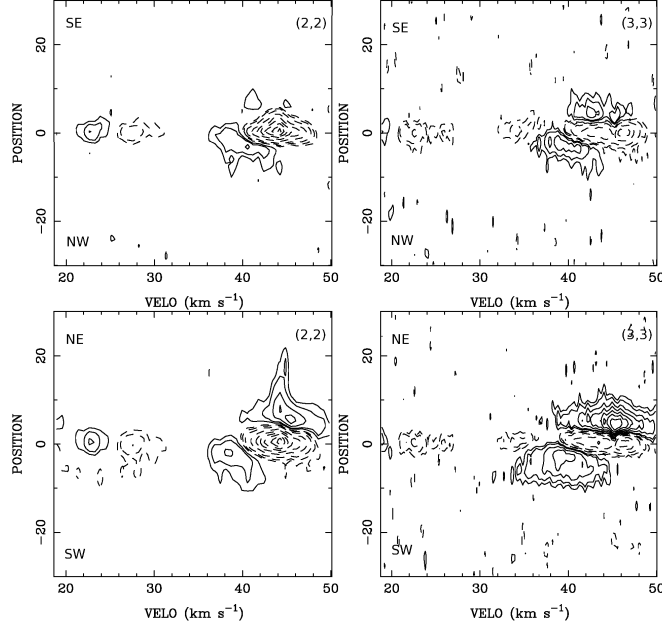


FIG. 5.— Position-velocity diagrams of NH_3 (2,2) and (3,3) from the VLA-D data. The cuts were done at $\text{PA}=45^\circ$ (bottom row) and $\text{PA}=135^\circ$ (top row). Dashed contours are absorption, solid contours are emission. Contouring is at $-168, -144, -120, -96, -72, -48, -36, -24, -12, -4, 4, 8, 12, 16, 24, 32, 40, 48, 56, 64 \times 1 \text{ mJy beam}^{-1}$. Only one inner satellite line is covered in the velocity range. In the SW-NE cuts (across the major axis of the cloud) the difference in the velocity of the emission with respect to $V_{sys} = 42 \text{ km s}^{-1}$ increases closer to the position center. This can be interpreted as spin up with decreasing distance from the center. However, the same trend is present in the NW-SE cuts (along the minor axis of the cloud), although only in the stronger, blueshifted side of the emission. This suggests that besides rotation, radial motions in the frame of the central stars are also present.

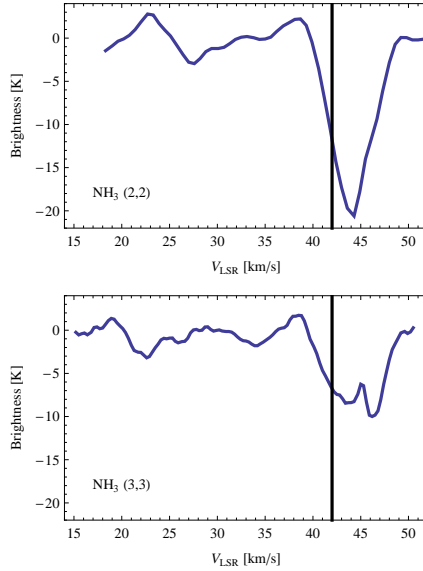


FIG. 6.— NH_3 spectra from the VLA-D observations toward the center of the absorption in G20.08N. The vertical line marks the systemic velocity ($V_{sys} = 42 \text{ km s}^{-1}$). The small peak near the middle of the (3,3) absorption is due to maser emission (confirmed in the high-resolution, VLA-BnA data, see §3.6). The absorption peaks in the main (2,2) and (3,3) lines are redshifted with respect to V_{sys} , indicating the presence of inflow in the kinematics of the parsec-scale molecular cloud. The other weak absorption component seen in the (2,2) spectrum is one of the inner satellites. The absorption component at $\approx 22 \text{ km s}^{-1}$ in the (3,3) spectrum is also an inner satellite. The weaker absorption at $30 - 37 \text{ km s}^{-1}$ in the (3,3) spectrum may arise from an outflow. The blueshifted absorption in the main lines closest to V_{sys} might arise from blending with the rotation seen in emission.

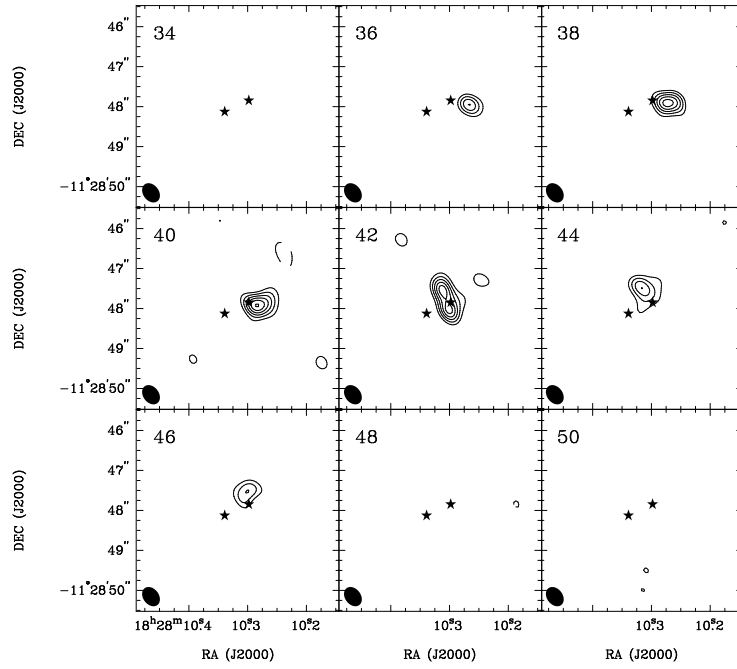


FIG. 7.— Channel maps of OCS $J = 19 - 18$ from the SMA-VEX observations. Contours are $-4, 4, 6, 8, 10, 12, 14 \times 30$ mJy beam $^{-1}$ (negative in *dashed*, and positive in *solid*). The peak intensity is 423 mJy beam $^{-1}$. The numbers in the upper left corner indicate the central LSR velocity of the channel. The two stars mark the positions of H II regions A (west) and B (east).

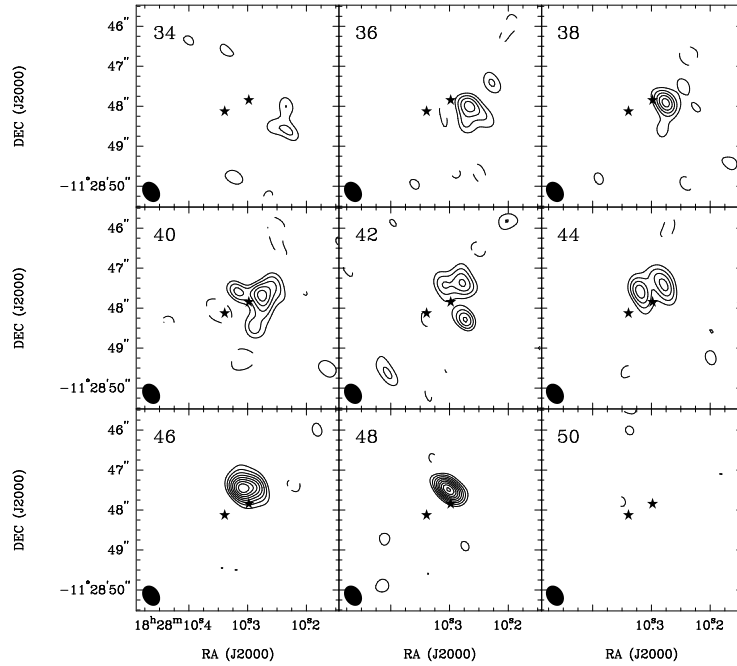


FIG. 7 (CONTINUED).— Channel maps of SO₂ $J(K_a, K_b) = 11(1, 11) - 10(0, 10)$ from the SMA-VEX observations. Contours are $-4, 4, 6, 8, 10, 12, 14, 16, 18, 20 \times 30$ mJy beam $^{-1}$ (negative in *dashed*, and positive in *solid*). The peak intensity is 612 mJy beam $^{-1}$.

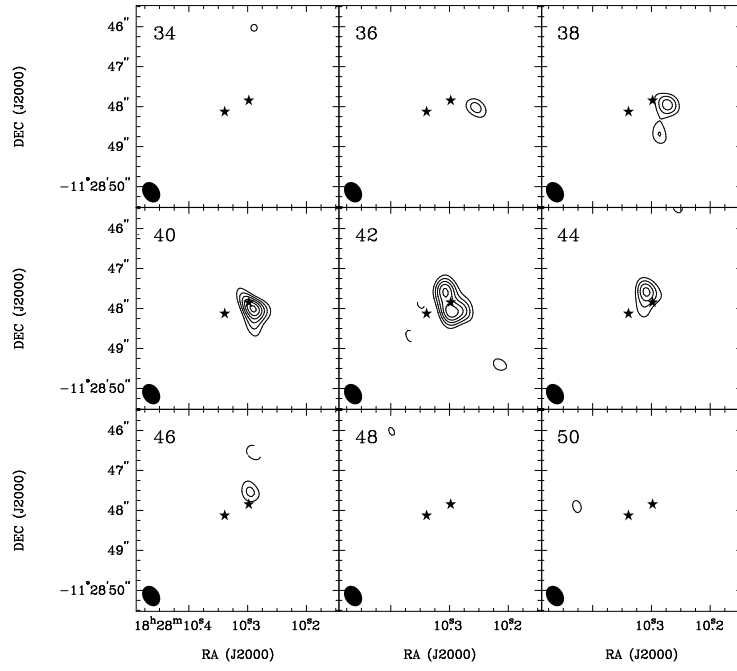


FIG. 7 (CONTINUED).— Channel maps of $\text{CH}_3\text{CN } J(K) = 12(3)-11(3)$ from the SMA-VEX observations. Contours are $-4, 4, 6, 8, 10, 12, 14 \times 30 \text{ mJy beam}^{-1}$ (negative in *dashed*, and positive in *solid*). The peak intensity is $440 \text{ mJy beam}^{-1}$.

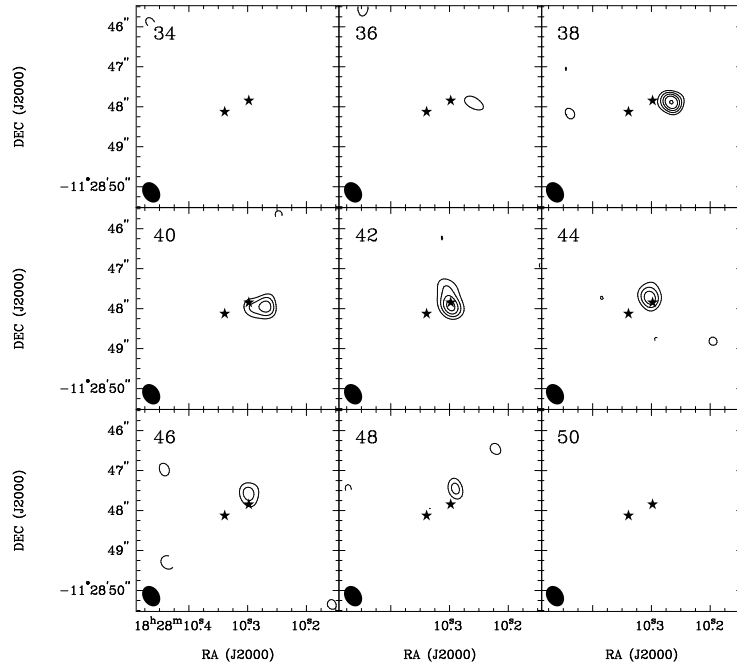


FIG. 7 (CONTINUED).— Channel maps of $\text{CH}_3\text{CN } J(K) = 12(4)-11(4)$ from the SMA-VEX observations. Contours are $-4, 4, 6, 8, 10, 12, 13 \times 30 \text{ mJy beam}^{-1}$ (negative in *dashed*, and positive in *solid*). The peak intensity is $401 \text{ mJy beam}^{-1}$.

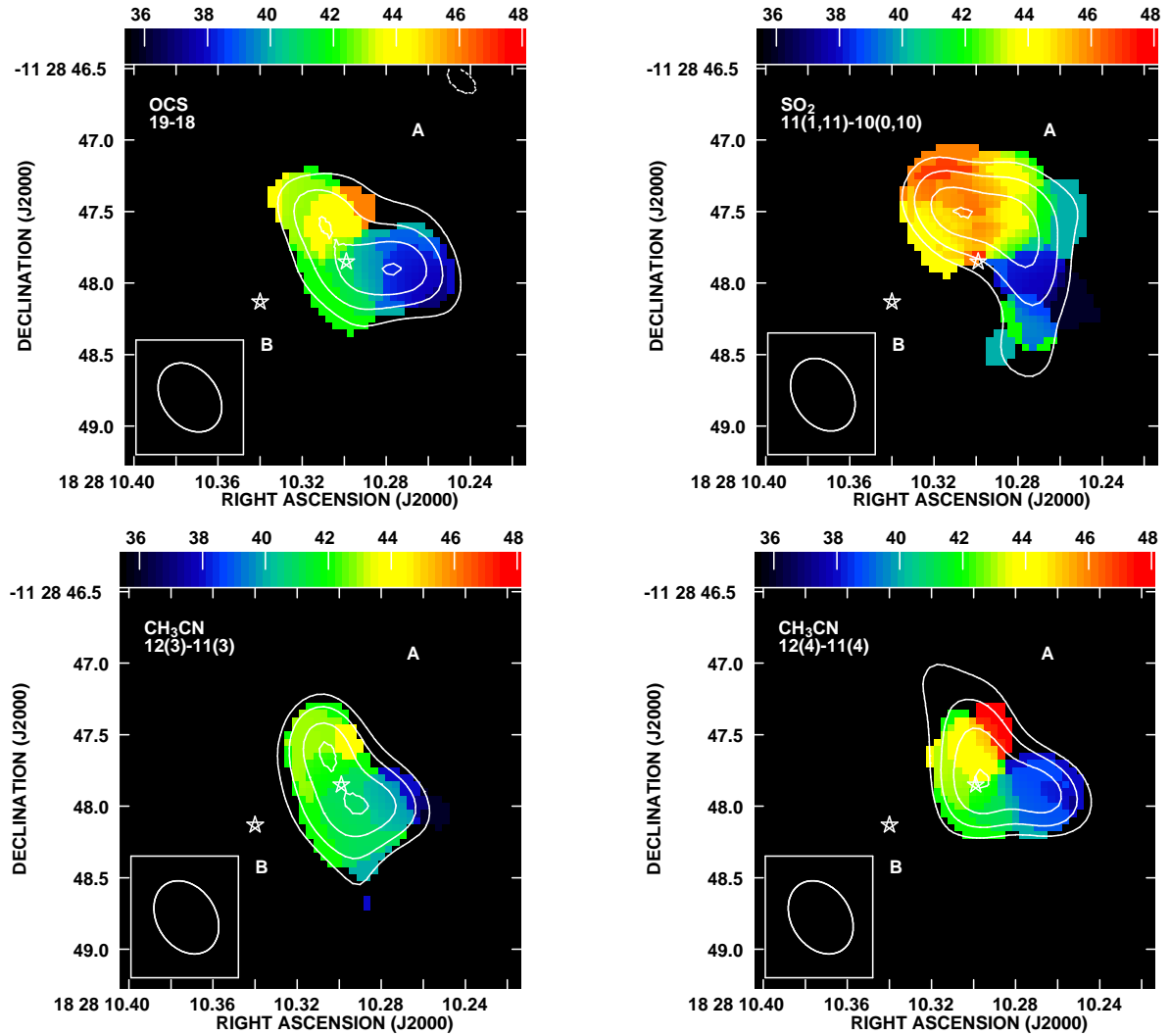


FIG. 8.— Velocity-integrated emission (moment 0, *contours*) and intensity-weighted mean velocity (moment 1, *color scale*) maps from hot-core molecules toward G20.08N. The *Top Left* panel shows the OCS $J = 19 - 18$ (contours are $-5, 5, 9, 13, 17 \times 0.15 \text{ Jy beam}^{-1} \text{ km s}^{-1}$). The *Top Right* panel corresponds to the SO_2 $J(K_a, K_b) = 11(1, 11) - 10(0, 10)$ (contours are $-5, 5, 8, 12, 15 \times 0.25 \text{ Jy beam}^{-1} \text{ km s}^{-1}$). The *Bottom Left* panel shows the CH_3CN $J(K) = 12(3) - 11(3)$ (contours are $-5, 5, 8, 12, 15 \times 0.15 \text{ Jy beam}^{-1} \text{ km s}^{-1}$). The *Bottom Right* panel plots the CH_3CN $J(K) = 12(4) - 11(4)$ (contours are $-5, 5, 9, 14, 19 \times 0.1 \text{ Jy beam}^{-1} \text{ km s}^{-1}$). Negative contours are in *dashed* style, and positive contours in *solid*. Only the continuum H II region A is associated with warm gas in our SMA-VEX data. The extent of the line emission is similar in all the tracers, although for the SO_2 it is more extended toward the northwest and more absorbed toward the continuum peak. The velocity gradient seen in the channel maps for each molecule is also seen here. The color scale is the same in all the frames.

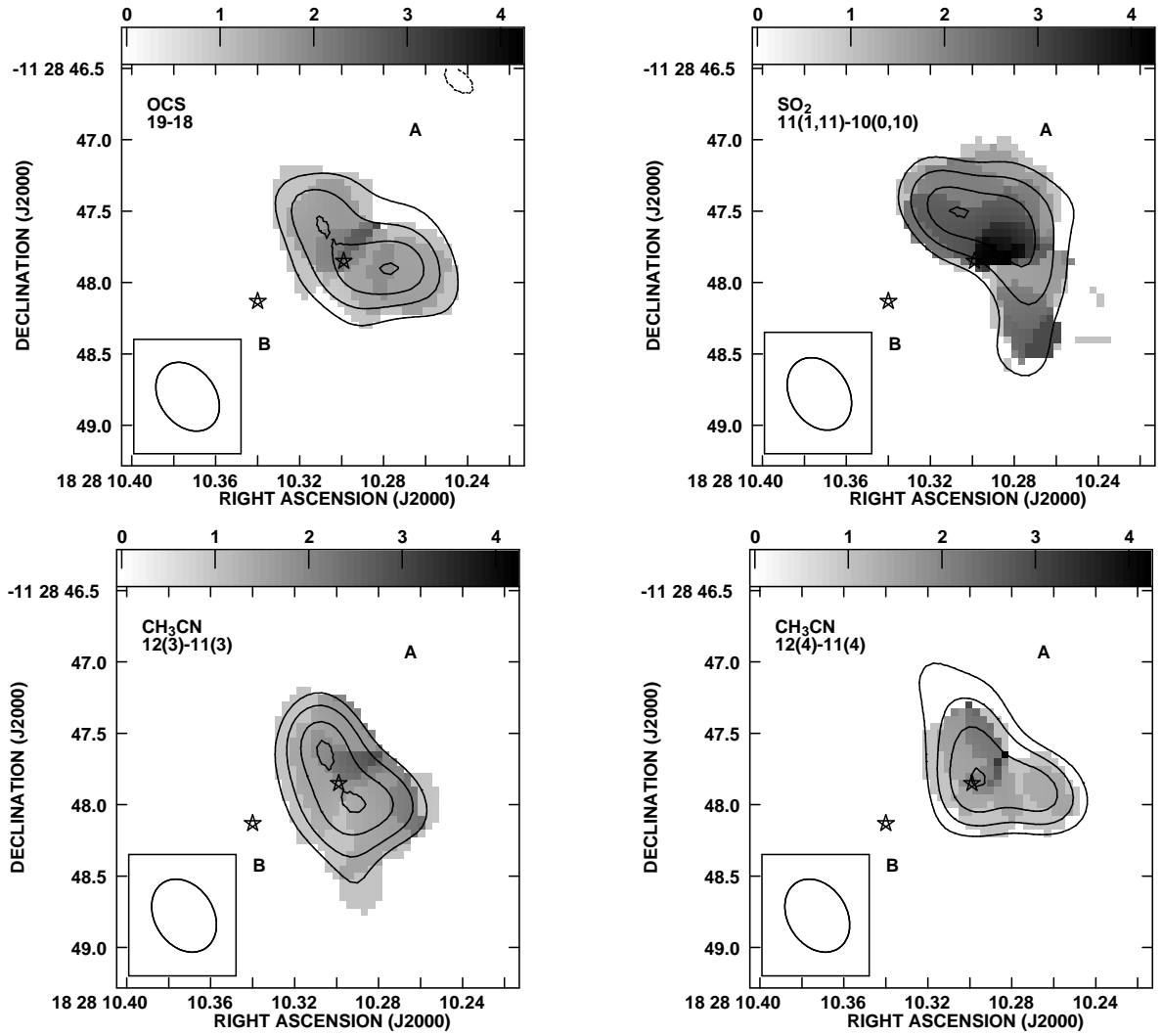


FIG. 9.— Velocity-integrated emission (moment 0, *contours*) and velocity dispersion with respect to moment-1 velocity (moment 2, *gray scale*) maps from hot-core molecules toward G20.08N. Contours are the same as in Fig. 8. The plotted velocity dispersion is $\sigma = \text{FWHM}/2(2 \ln 2)^{1/2}$. σ increases toward the center of H II region A, possibly caused by unresolved motions toward the center.

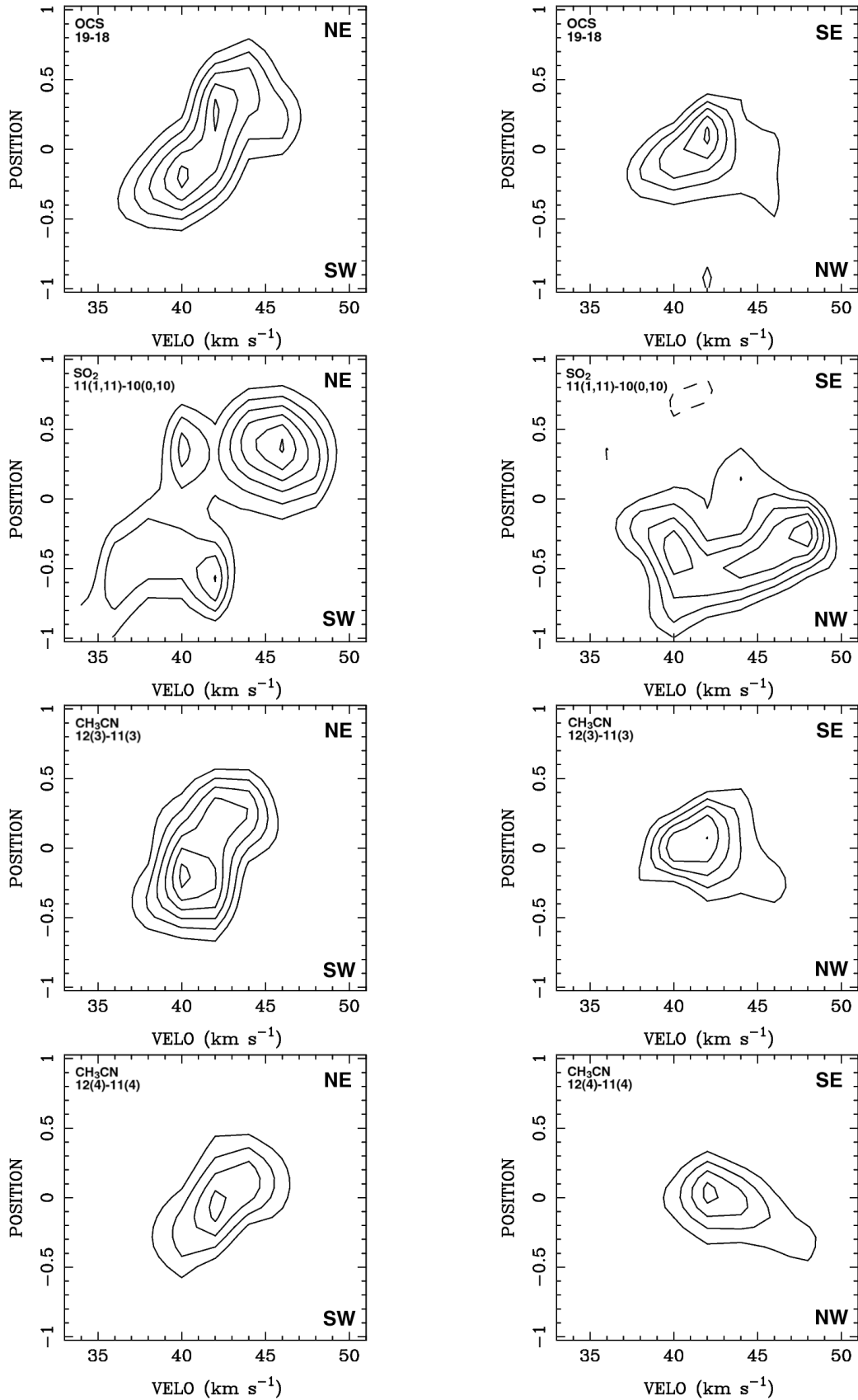


FIG. 10.— Position-velocity diagrams of the SMA-VEX observations. The *left* column is for a cut at PA= 45° (SW-NE). The *right* column is at PA= 135° (NW-SE). Cuts are centered at the position of the continuum peak of H II region A. Contours are the same as in Fig. 7. The velocity gradient interpreted as rotation from SW to NE is clearly seen in OCS and CH₃CN. The SO₂ features are more complex.

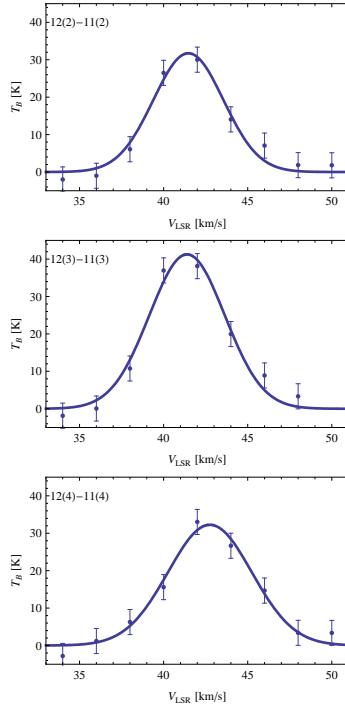


FIG. 11.— Spectra (*points*) and Gaussian fits (*lines*) to the $\text{CH}_3\text{CN } J = 12 - 11, K = 2, 3, \text{ and } 4$ lines at the position of H II region A. Error bars denote the 1σ noise in the 2 km s^{-1} -wide channels.

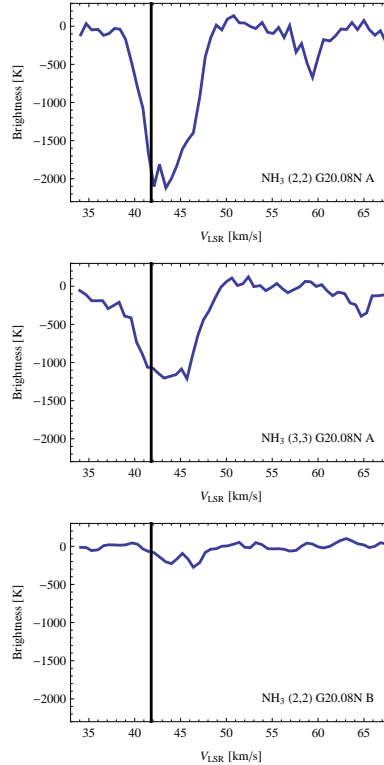


FIG. 12.— *Top* and *middle* panels: $\text{NH}_3 (2,2)$ and $(3,3)$ spectra toward the absorption peak of H II region A in the VLA-BnA observations. The vertical line marks the systemic velocity ($V_{\text{sys}} = 41.8 \text{ km s}^{-1}$) of the molecular gas at scales comparable to the H II region. The centers of the absorption lines are redshifted with respect to V_{sys} , indicating inflow of molecular gas toward H II region A at small scales. The $(3,3)$ absorption is broader ($\text{FWHM} \approx 6.5 \text{ km s}^{-1}$) than the $(2,2)$ ($\text{FWHM} \approx 5.6 \text{ km s}^{-1}$), probably caused by larger motions closer to the center. *Bottom* panel: $\text{NH}_3 (2,2)$ spectrum toward H II region B. The absorption, considerably fainter than for H II region A, is also redshifted.

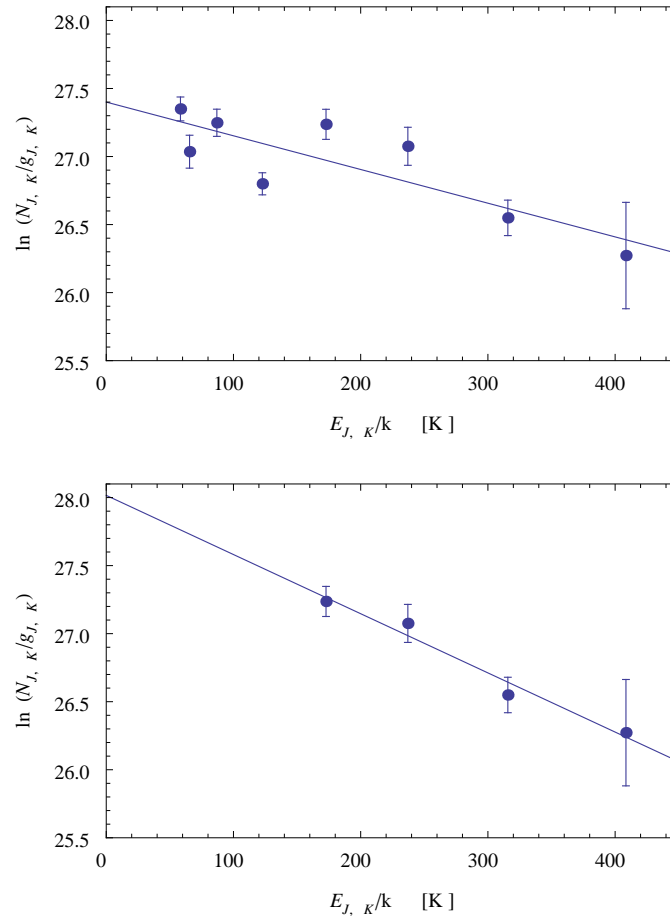


FIG. 13.— Rotation diagram for the $\text{CH}_3\text{CN } J=12-11$. The *top* panel is a fit of all the $K=0, \dots, 7$ lines. The *bottom* panel uses only the $K=4, \dots, 7$ lines, which have lower optical depths. Error bars are 3σ values. Lines are the linear fits to the data.

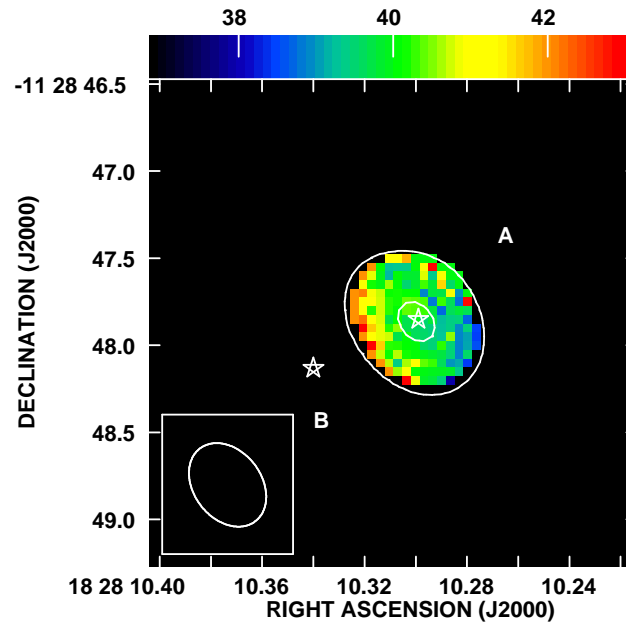


FIG. 14.— Velocity-integrated emission (moment 0, *contours*) and intensity-weighted mean velocity (moment 1, *color scale*) map of the $\text{H}30\alpha$ RRL emission toward G20.08N. Contours are at $7, 50 \times 0.5 \text{ Jy beam}^{-1} \text{ km s}^{-1}$. Although the emission is unresolved at half power, the moment 1 map hints at the presence of a velocity gradient in the ionized gas similar to that seen in CH_3CN and OCS .

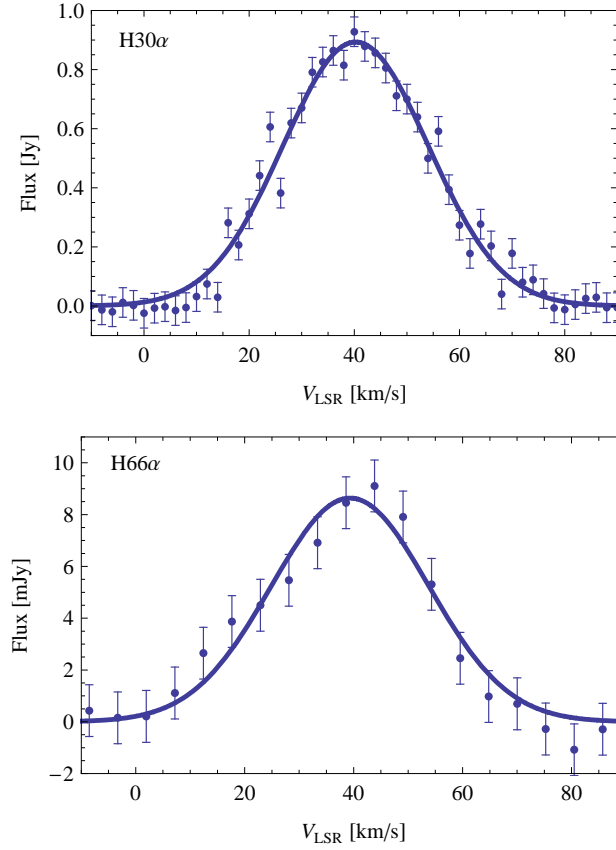


FIG. 15.— Spectra (*points*) and Gaussian fits (*lines*) to the H30 α (*top panel*) and H66 α (*bottom panel*) lines toward G20.08N A. Error bars denote the 1σ noise in the channels. The channel spacing is 2 km s^{-1} for H30 α and 5.2 km s^{-1} for H66 α . The flux was integrated over a $0.5''$ square box centered on H II region A.

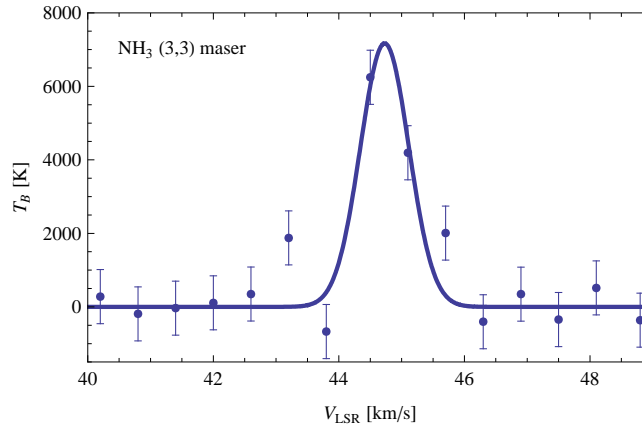


FIG. 16.— VLA-BnA spectrum of the NH₃ (3,3) maser spot toward G20.08N. The brightness temperature T_B scale assumes an angular size equal to half the uniform-weighted beam dimensions.